Article

A single-cell atlas of human and mouse white adipose tissue

https://doi.org/10.1038/s41586-022-04518-2

Received: 15 May 2021

Accepted: 4 February 2022

Published online: 16 March 2022

Check for updates

Margo P. Emont[1,2], Christopher Jacobs[1,2], Adam L. Essene[1], Deepti Pant[1], Danielle Tenen[1,2], Georgia Colleluori[3], Angelica Di Vincenzo[3], Anja M. Jørgensen[4], Hesam Dashti[2], Adam Stefek[2], Elizabeth McGonagle[2], Sophie Strobel[2], Samantha Laber[2], Saaket Agrawal[2,5], Gregory P. Westcott[1], Amrita Kar[1,2], Molly L. Veregge[1], Anton Gulko[1], Harini Srinivasan[1,2], Zachary Kramer[1], Eleanna De Filippis[6], Erin Merkel[1], Jennifer Ducie[7], Christopher G. Boyd[8], William Gourash[9], Anita Courcoulas[9], Samuel J. Lin[10], Bernard T. Lee[10], Donald Morris[10], Adam Tobias[10], Amit V. Khera[2,5,11], Melina Claussnitzer[2,12], Tune H. Pers[4], Antonio Giordano[3], Orr Ashenberg[13], Aviv Regev[13,14,15], Linus T. Tsai[1,2,11] & Evan D. Rosen[1,2,11]✉

White adipose tissue, once regarded as morphologically and functionally bland, is now recognized to be dynamic, plastic and heterogenous, and is involved in a wide array of biological processes including energy homeostasis, glucose and lipid handling, blood pressure control and host defence[1]. High-fat feeding and other metabolic stressors cause marked changes in adipose morphology, physiology and cellular composition[1], and alterations in adiposity are associated with insulin resistance, dyslipidemia and type 2 diabetes[2]. Here we provide detailed cellular atlases of human and mouse subcutaneous and visceral white fat at single-cell resolution across a range of body weight. We identify subpopulations of adipocytes, adipose stem and progenitor cells, vascular and immune cells and demonstrate commonalities and differences across species and dietary conditions. We link specific cell types to increased risk of metabolic disease and provide an initial blueprint for a comprehensive set of interactions between individual cell types in the adipose niche in leanness and obesity. These data comprise an extensive resource for the exploration of genes, traits and cell types in the function of white adipose tissue across species, depots and nutritional conditions.

An atlas of human white adipose tissue

Mature adipocytes are too large and fragile to withstand traditional single-cell approaches. As a result, several groups have focused on the non-adipocyte stromal-vascular fraction (SVF) of mouse[3–6] and human[7] adipose tissue. An alternative strategy involves single-nucleus sequencing (sNuc-seq), which can capture adipocytes, and has been used to describe mouse white[8,9] and human brown adipose tissue[10]. To compare these approaches in the context of human white adipose tissue (WAT), we pursued experiments on two cohorts of subjects. In the first, we collected subcutaneous WAT from nine women, isolated single cells from the SVF using collagenase digestion, and then performed whole-cell Drop-seq (hereafter referred to as single-cell RNA sequencing (scRNA-seq)). Because different depots have been differentially linked to metabolic disease[11], for the second cohort we collected paired subcutaneous (SAT) and visceral (VAT) adipose tissue from ten individuals and SAT alone from three additional individuals (ten women and three men), and performed sNuc-seq (Fig. 1a, b, Extended Data Table 1). Doublet and low-quality filtering left 166,149 total cells (28,465 single cells and 137,684 single nuclei). The data from both approaches were integrated, enabling the identification of the canonical cell types found in WAT, including adipocytes, adipose stem and progenitor cells (ASPCs), vascular cells and immune cells (Fig. 1c, d, Supplementary Table 1). As expected, adipocytes were found only in the sNuc-seq dataset. The sNuc-seq data were also enriched for vascular cells and macrophages, probably because collagenase digestion did not fully dissociate these cell types. Mesothelial cells were not detected in the scRNA-seq dataset, which did not include visceral tissue. Some of the visceral samples included cells that appeared to be endometrial in origin (*PRLR*+), probably owing to endometriosis. Overall proportions of adipocytes and ASPCs did not differ between depots, but depot clearly affects the distribution of cells within these populations (Extended Data Fig. 1a, b,

[1]Division of Endocrinology, Diabetes and Metabolism, Beth Israel Deaconess Medical Center, Boston, MA, USA. [2]Broad Institute of MIT and Harvard, Cambridge, MA, USA. [3]Department of Experimental and Clinical Medicine, Center of Obesity, Marche Polytechnic University, Ancona, Italy. [4]Novo Nordisk Foundation Center for Basic Metabolic Research, University of Copenhagen, Copenhagen, Denmark. [5]Center for Genomic Medicine, Department of Medicine, Massachusetts General Hospital, Boston, MA, USA. [6]Division of Endocrinology, Diabetes and Metabolism, Mayo Clinic Scottsdale, AZ, USA. [7]Division of Gynecologic Oncology, Department of Obstetrics and Gynecology, Beth Israel Deaconess Medical Center, Boston, MA, USA. [8]Department of Surgery, Beth Israel Deaconess Medical Center, Boston, MA, USA. [9]Department of Surgery, University of Pittsburgh Medical Center, Pittsburgh, PA, USA. [10]Division of Plastic Surgery, Department of Surgery, Beth Israel Deaconess Medical Center, Boston, MA, USA. [11]Harvard Medical School, Boston, MA, USA. [12]Diabetes Unit and Center for Genomic Medicine, Massachusetts General Hospital, Boston, Massachusetts, USA. [13]Klarman Cell Observatory, Broad Institute of MIT and Harvard, Cambridge, MA, USA. [14]Howard Hughes Medical Institute, Koch Institute of Integrative Cancer Research, Department of Biology, Massachusetts Institute of Technology, Cambridge, MA, USA. [15]Genentech, South San Francisco, CA, USA. ✉e-mail: erosen@bidmc.harvard.edu

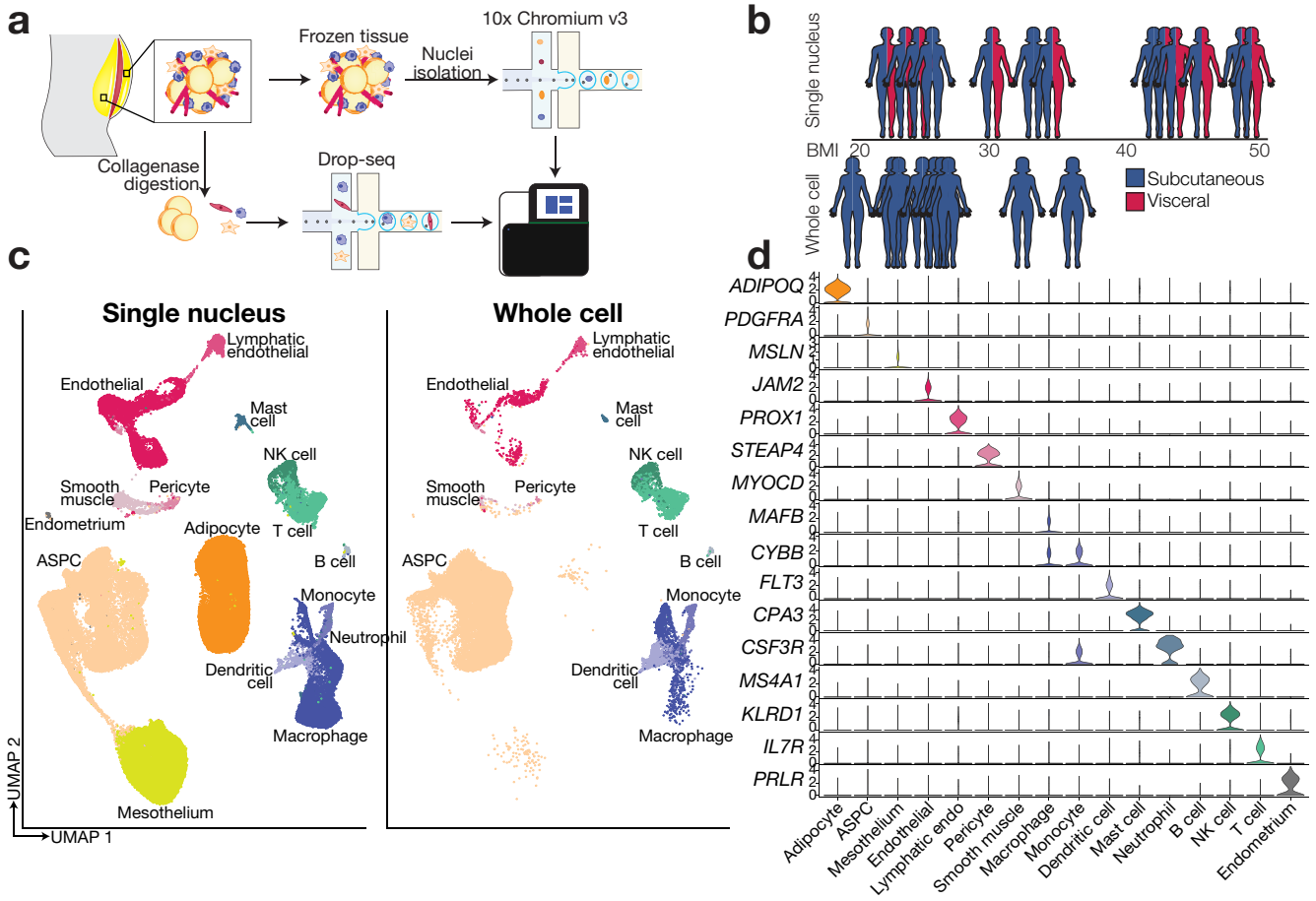

Fig. 1 | A single-cell atlas of human white adipose tissue. a, Schematic of workflows for scRNA-seq and sNuc-seq of human WAT. **b**, Graphical representation of the cohorts for both studies. Only the sNuc-seq cohort contains VAT. **c**, Uniform manifold approximation and projection (UMAP) projection of all 166,129 sequenced human cells split by cohort. **d**, Marker genes for each cell population in the human WAT dataset. **e**, Schematic of workflow for sNuc-seq of mouse ING and PG adipose tissue. **f**, UMAP projection of all 197,721 sequenced mouse cells split by diet. **g**, Marker genes for each cell population in the mouse WAT dataset.

Extended Data Table 2, Supplementary Fig. 1). In our limited cohort, we could not detect major effects of body mass index (BMI) on cell-type proportions. To assess this finding at larger scale, we used our dataset as a reference to estimate cell-type proportions in bulk RNA-sequencing data[12] obtained from the SAT of 331 men in the METSIM cohort[13]. This deconvolution analysis showed that the relative abundance of adipocytes in that cohort was negatively correlated with BMI, whereas ASPCs and myeloid cells were positively correlated (Extended Data Fig. 1c).

An atlas of mouse white adipose tissue

Mouse models are commonly used to study adipose tissue biology[14]. We thus sought to compare mouse and human WAT at the single-cell level by performing sNuc-seq on inguinal adipose tissue (ING) (corresponding to human SAT) and perigonadal adipose tissue (PG) (epididymal (EPI) in males and periovarian (POV) in females, corresponding to human VAT) of mice fed either a chow or high-fat diet (HFD) for 13 weeks (Fig. 2a, b). After doublet removal and quality filtering, we considered a total of 197,721 cells (106,469 from PG and 91,252 from ING), identifying all cell types observed in human WAT (Fig. 2c, d, Supplementary Table 2) with the addition of distinct male and female epithelial populations (*Dcdc2a*+ and *Erbb4*+, respectively). The female population is largely found in ING samples and resembles mammary epithelial cells, whereas the male population is almost exclusively found in PG samples, and as noted by others[9] may represent contaminants from the epididymis and other reproductive structures that are tightly apposed to fat[15]. In contrast to the human data, cell-type abundance in mouse WAT is highly dependent on body weight, with relatively little variation between depots (Fig. 2c, Extended Data Fig. 2a, b, Extended Data Table 2). The proportions of cell types in mouse adipose tissue after HFD were notably different between male and female mice, which might reflect a true sex difference or may reflect higher weight gain in males (Extended Data Fig. 2b). To compare across species, we used a reference mapping algorithm to assign each mouse cell to a human cluster and noted a high degree of overall similarity between annotated mouse clusters and mapped human clusters (Extended Data Fig. 2c).

Vascular cells

Subclustering of human vascular cells revealed expected cell types, including blood endothelial clusters that represent arteriolar, stalk and venular cells, as well as lymphatic endothelial cells, pericytes and smooth muscle cells (Extended Data Fig. 3a, b). Mouse vascular cells formed similar clusters (Extended Data Fig. 3c, d). As expected, reference mapping demonstrated high similarity between human and mouse vascular subclusters (Extended Data Fig. 3e) and proportions of subclusters were similar across species (Extended Data Fig. 3f, g).

Immune cells

Analysis of human immune cells from scRNA-seq and sNuc-seq samples again revealed expected cell types, including multiple subpopulations of monocytes, macrophages (*CD14*+), dendritic cells, B and T

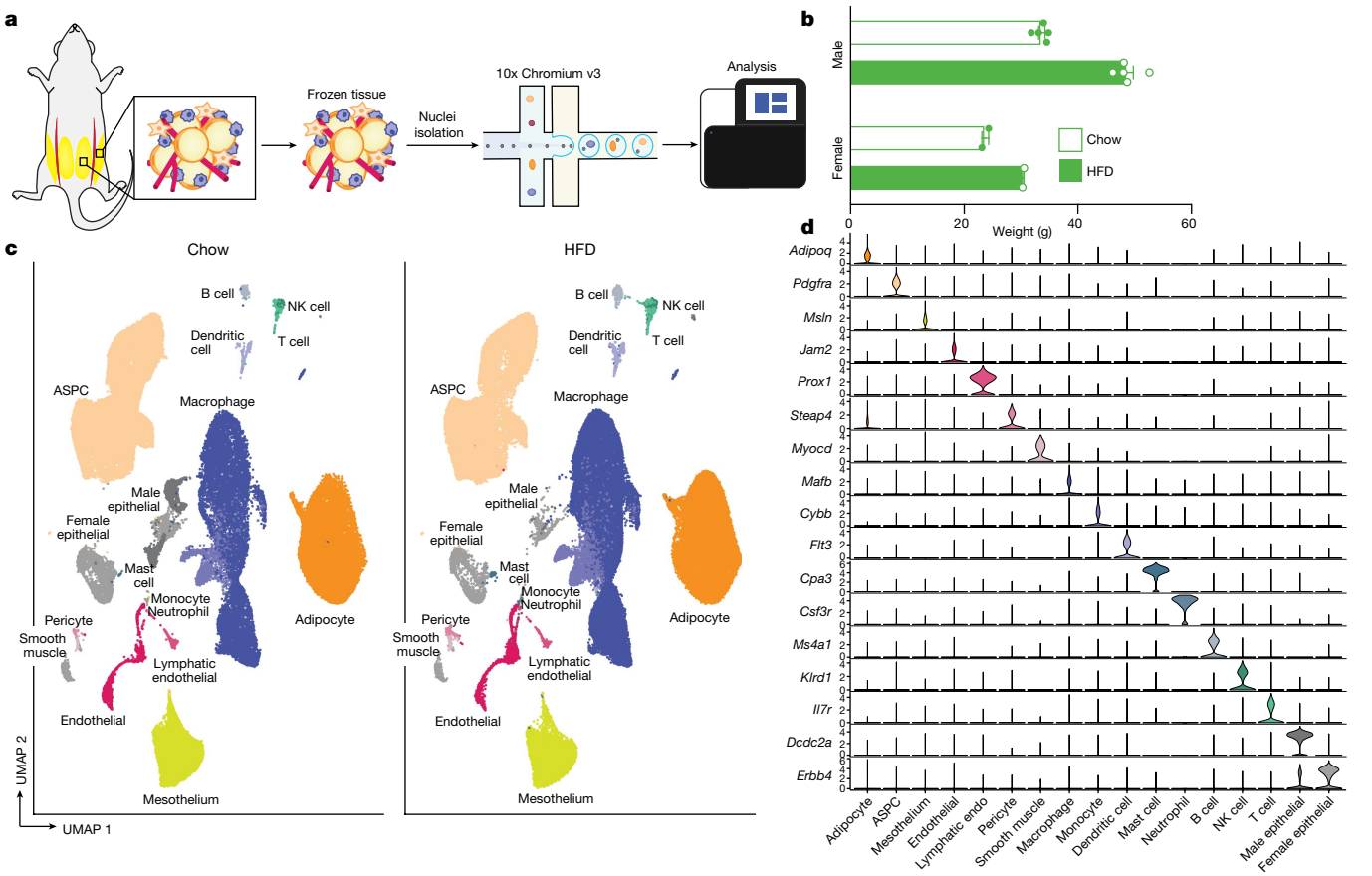

Fig. 2 | A single cell atlas of mouse white adipose tissue. a, Schematic of workflow for sNuc-seq of mouse ING and PG adipose tissue. **b**, Body weight of chow and high-fat fed animals used for sNuc-seq (n = 5 chow and 5 HFD male mice, 2 chow and 2 HFD female mice). Error bars represent standard error of the mean (SEM). **c**, UMAP projection of all 197,721 sequenced mouse cells split by diet. **d**, Marker genes for each cell population in the mouse WAT dataset.

lymphocytes, and natural killer (NK) cells (*CD96*+), mast cells (*CPA3*+), and neutrophils (*CSF3R*+) (Extended Data Fig. 4a, b). Monocyte subpopulations 1 and 2 resemble classical and non-classical monocytes and DC subpopulations 1 and 2 resemble previously reported *CLEC9A*+ and *CD1C*+ populations from blood, respectively[16]. Lymphocytes also resemble previously reported B cell, T cell and NK cell populations from human WAT, including *CTLA4*+ human regulatory T cells[17]. Examination of the mouse WAT immune compartment revealed most of the same cell types, although there were notable differences in the relative abundance of myeloid and lymphoid cells between species (Extended Data Fig. 4c, d). Human WAT contains somewhat fewer T and NK cells than macrophages or monocytes (approximately 30% versus 60% of recovered immune cells); this imbalance was greatly exaggerated in mouse WAT (macrophages were approximately 90% of recovered immune cells versus 3% T and NK cells). Because a wealth of data supports a key role for macrophages and monocytes in adipose biology[18,19], we separated these cell types from other immune cells in silico for subsequent analysis. Mouse clusters of non-monocytes and non-macrophages mapped relatively well to their human counterparts, with some mixing of T and NK populations (Extended Data Fig. 4e). Macrophages and monocytes also mapped well to their general class, but this association often broke down when considering macrophage subpopulations (Extended Data Fig. 4f).

The proportion of immune cell populations was similar in human SAT and VAT, with a few exceptions (Extended Data Fig. 5a, e). In mice, small depot-dependent differences were eclipsed by relatively huge shifts in response to diet in male mice (Extended Data Fig. 5b, d, f). Most notably, HFD resulted in a massive increase in macrophage numbers, primarily in PG, consistent with a large body of prior data[18,20] (Extended Data Figs. 2b, 5f). Reductions in the proportion of most other immune cell types (for example, NK cells, T and B lymphocytes, dendritic cells and neutrophils) are probably due to the large increase in macrophages, rather than to intrinsic loss of those specific cell types following HFD (Extended Data Fig. 5b, d, f). Mast cells increase proportionally after HFD, as previously reported[21] (Extended Data Fig. 5f).

Accumulation of adipose tissue macrophages in obesity has also been shown in human WAT, using a combination of histomorphometry and flow sorting[19,22]. Our data generally support this conclusion, although the magnitude of the effect is substantially less prominent than that seen in mouse WAT (Extended Data Fig. 1b, 5c, e, f). The largest change involves the hMac3 cluster, which is induced in visceral fat with higher BMI (Extended Data Fig. 5c, e).

Mesothelial cells

Subclustering of mesothelial cells revealed three populations in both human VAT and mouse PG (Extended Data Fig. 6a–d). When mouse mesothelial clusters were mapped to human clusters, cells were split between human clusters hMes1 and hMes2, with no cells mapping to hMes3 (Extended Data Fig. 6e). The proportions of most mesothelial subpopulations did not vary with obesity or HFD, with the exception of hMes1 and hMes2, which were reduced and increased in higher BMIs, respectively (Extended Data Fig. 6f, g).

ASPCs

We identified six distinct subpopulations of human ASPCs (see Supplementary Note 1) in subclustered scRNA-seq and sNuc-seq samples,

all of which express the common marker gene *PDGFRA* (Extended Data Fig. 7a, b). Similarly, we noted six subpopulations in the mouse ASPC data, all of which were also *Pdgfra*+ and some of which correspond well with a particular human subpopulation (Extended Data Fig. 7c–e). For example, mASPC2 and hASPC2 are characterized by high expression of *Aldh1a3* and *ALDH1A3*, respectively, and strongly resemble previously identified early multipotent progenitor cells that reside in the reticular interstitium of the fat pad[5]. Similarly, mASPC4 and hASPC4 express *Epha3* and *EPHA3*, respectively, and probably represent the anti-adipogenic 'adipogenesis-regulatory' cells (Aregs) population reported by Schwalie et al.[3]. Seeking to better place our mouse ASPC data into the overall context of the published literature, we integrated our data with those reported by others[3–6,9] and found that ASPC populations identified by individual studies were generally preserved after integration, suggesting robustness of these clusters. Specifically, the previously described *Icam1*+ committed progenitor, *Dpp4*+ early progenitor and *Cd142*+ Areg populations[23] cluster together across studies (Extended Data Fig. 7f).

Many human and mouse ASPC subclusters showed dependency on diet, depot or both. hASPC1, hASPC4 and hASPC5 were more prevalent in SAT than VAT, with increases in SAT hASPC4 and hASPC5 proportion in subjects with higher BMI (Extended Data Fig. 8a, c, e). Conversely, hASPC3 and hASPC6 were more prevalent in VAT. In male mice, early progenitor cells (mASPC2) were notably more abundant in ING than PG and mASPC5 and mASPC6 were more prevalent in EPI versus ING, although this varied with obesity (Extended Data Fig. 8b, d, f). Many of these observations are consistent with previous findings. For example, HFD has been shown to increase adipogenesis specifically in PG in mice[24,25]. Our data indicate that pre-adipocyte subclusters such as mASPC6 increase markedly in response to HFD in PG only. The loss of early progenitors (mASPC2) in PG with HFD is consistent with conversion of these cells along the differentiative pathway, that is, towards mASPC6 (Extended Data Fig. 8b, d, f).

Unique populations of human adipocytes

White adipocytes are generally considered to be monotypic and essentially uniform in function, although some recent studies have begun to challenge this assumption[8–10,26]. The high resolution of our data enabled us to find that human white adipocytes cluster into seven subpopulations with distinct markers (Fig. 3a, b). We noted strong depot-specific associations of adipocyte subtypes, with hAd1, hAd3, hAd4 and hAd7 localized primarily to SAT, whereas hAd2 and hAd6 were almost exclusively found in VAT. hAd5 represents a smaller population that is roughly equally distributed between SAT and VAT (Extended Data Fig. 9a–c). We also noted a BMI-dependent shift in adipocyte subtype within both depots (Extended Data Fig. 9b, c). Notably, all adipocyte subpopulations are present in the majority of subjects, indicating that these subtype designations are generalizable and do not reflect sample-specific variation (Extended Data Fig. 9c). Immunohistochemistry and/or immunofluorescence of markers for hAd4, hAd5, hAd6 and hAd7 in human SAT or VAT identified specific subpopulations of adipocytes at proportions similar to those seen in the single-cell data (Fig. 3c, Extended Data Fig. 9d, e). To examine whether SAT subtype proportion was influenced by BMI in a larger dataset, we estimated individual subtype proportions by deconvolution analysis of bulk RNA-seq data from purified isolated subcutaneous human adipocytes from 43 women (Fig. 3d). This analysis showed that clusters hAd4 and hAd7 trend to negative correlation with BMI, aligning with our immunohistochemistry findings, whereas hAd5 proportion is positively correlated with BMI. Visceral adipocytes are absent from this dataset and so we were unable to assess the prevalence of hAd2 or hAd6 in this cohort, although immunohistochemistry of the hAd6 marker EBF2 also suggests that its prevalence may be positively correlated with BMI (Fig. 3c).

A critical question is whether individual adipocyte subpopulations have specific functions. To assess this, we first looked at genes that participate in the major metabolic activities of adipocytes. All subpopulations expressed these genes, although their relative amounts differed. Thus, the adipokines adiponectin and adipsin (encoded by *CFD*) are most highly expressed in hAd3, and genes encoding insulin signalling components such as *INSR*, *IRS1* and *IRS2* are most highly expressed in hAd5 (Extended Data Fig. 9f). We next examined the data more holistically by performing pathway analysis for markers of each subpopulation (Extended Data Fig. 9g–m, Supplementary Table 3). The subpopulations hAd1 (which accounts for around 40% of SAT adipocyte nuclei) and hAd2 (which accounts for ~60% of VAT adipocyte nuclei) have relatively few specific markers, and the pathways that emerged were similarly generic (Extended Data Fig. 9g, h). These populations probably represent 'basal' subcutaneous or visceral adipocytes, so we therefore focused on subpopulations hAd3–hAd7 for more detailed analysis. hAd3 was associated with 'triglyceride biosynthesis' and included higher expression of *DGAT2*, *SREBF1* and *PNPLA3* (Extended Data Fig. 9i). The hAd4 cluster expresses the highest amounts of several fatty acid desaturases, including *ELOVL5* and *FADS3* (Extended Data Fig. 9j), which is particularly interesting in light of the insulin-sensitizing role of unsaturated lipokines such as palmitoleate[27]. hAd5 adipocytes, besides having the highest expression of several insulin signaling genes, were also characterized by expression of 'sphingolipid signalling genes' (Extended Data Fig. 9k). Both hAd3 and hAd4 exhibit high expression of lipogenic genes, whereas lipolytic gene expression is higher in hAd5 (Extended Data Fig. 9f).

We next investigated whether cultured human adipocytes retain evidence of subpopulation diversity. To this end, we used 57 RNA-seq datasets from human subcutaneous and visceral adipocyte progenitors differentiated ex vivo over a 14-day timecourse[28]. Deconvolution analysis revealed that many subpopulations identified in vivo were retained in culture. Furthermore, much of the previously noted depot selectivity was recapitulated, such that the visceral subpopulations hAd2 and hAd6 were more likely to appear in cultured visceral cells and the subcutaneous subpopulation hAd4 was overrepresented in cultured subcutaneous cells (Extended Data Fig. 10a). Furthermore, because these cultured samples were also subjected to high-content image-based profiling using LipocyteProfiler[28], we were able to correlate individual subpopulations with image-based features representing morphological and cellular phenotypes including lipid and mitochondrial content. Thus, ex vivo differentiated adipocyte cultures predicted to have high amounts of hAd3—associated with high lipogenic gene expression and lower lipolytic gene expression—have more overall lipid and larger lipid droplets (Fig. 3e, f). Conversely, ex vivo differentiated adipocyte cultures with high predicted hAd5 content have less overall lipid and smaller lipid droplets, consistent with a higher ratio of lipolytic to lipogenic gene expression (Extended Data Fig. 10b–d).

One particularly notable adipocyte subpopulation is hAd6, which selectively expresses genes typically associated with thermogenesis, such as *EBF2*, *ESRRG* and *PPARGC1A* (Extended Data Fig. 9l), a surprising finding given that this population is almost exclusively visceral (Fig. 3c, Extended Data Fig. 9a, c). To better understand the relationship between this subpopulation and visceral adiposity, we looked further into the hAd6 marker EBF2, which has previously been identified as a pro-thermogenic transcription factor[29]. Single nucleotide polymorphisms (SNPs) at the *EBF2* locus are associated with waist–hip ratio (WHR)[30], which could involve actions in either SAT or VAT. However, a recent genome-wide association study (GWAS) of loci associated with adiposity in specific depots[31] found a common variant 15 kb upstream of *EBF2* associated specifically with VAT (Extended Data Fig. 11a). Further analysis revealed that the minor allele of this SNP (minor allele frequency = 0.23) was associated with VAT adjusted for BMI and height (VATadj) (beta = 0.062 s.d. per allele, $P = 1.0 \times 10^{-12}$), but not adjusted abdominal subcutaneous (ASAT) (ASATadj: beta = −0.018 s.d. per

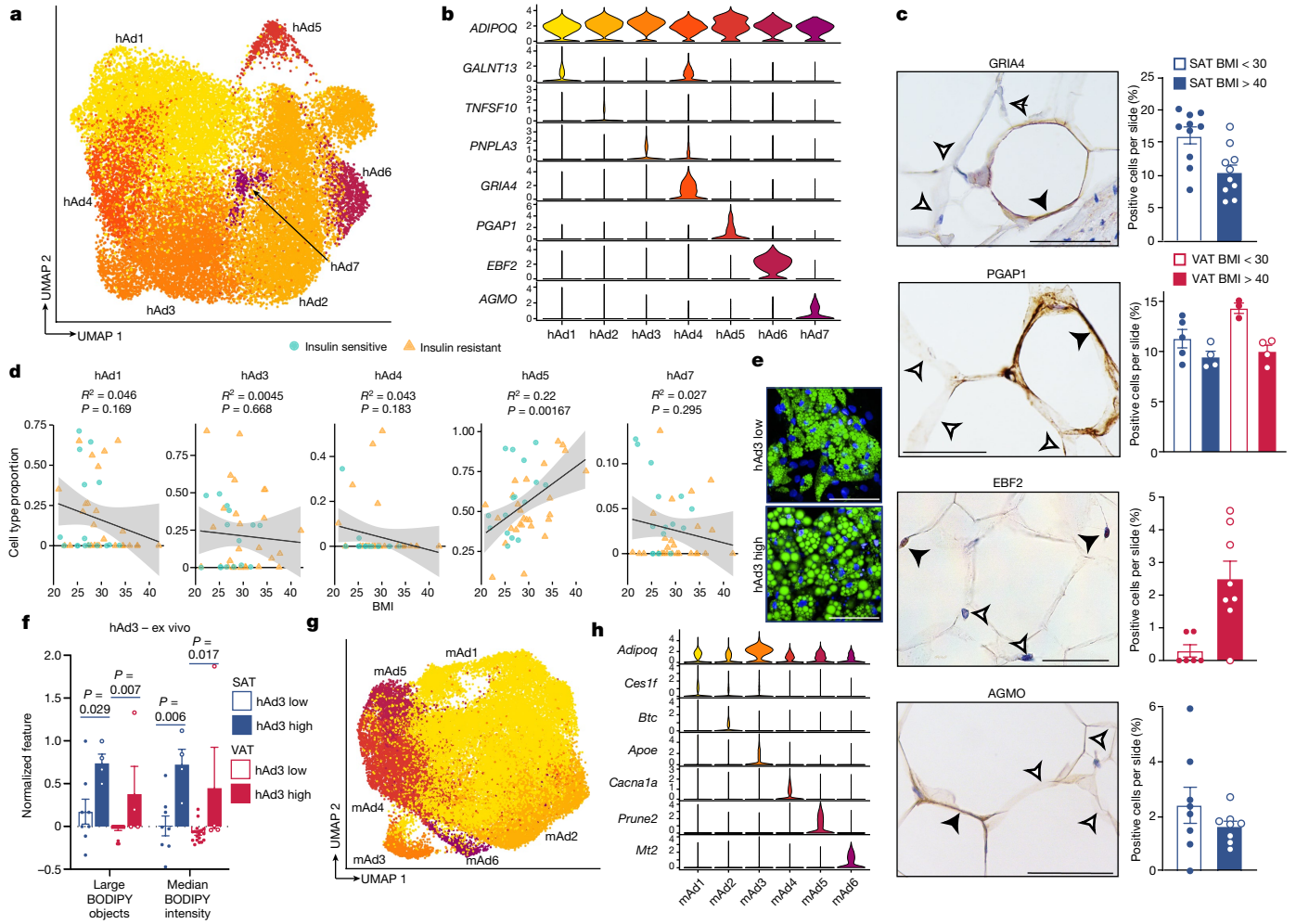

Fig. 3 | Subclustering of human and mouse adipocytes reveals multiple distinct populations that vary across depot and diet. a, UMAP projection of clusters formed by 25,871 human white adipocytes. **b**, Expression of adipocyte marker *ADIPOQ* and specific marker genes for each adipocyte subpopulation. **c**, Immunohistochemistry for marker genes of adipocyte subpopulations hAd4, hAd5, hAd6, and hAd7 in human adipose tissue and percentage of positive adipocytes per slide in lean and obese individuals (GRIA4: 5 lean, 5 obese, 2 slides each; PGAP1: 5 lean SAT, 4 obese SAT, 3 lean VAT, 4 obese VAT, 1 slide each; EBF2: 3 lean, 4 obese, 2 slides each; AGMO: 4 lean, 4 obese, 2 slides each). Scale bars: 25 µm for GRIA4, EBF2 and AGMO, 20 µm for PGAP1. **d**, Estimated proportions of adipocyte subpopulations in bulk RNA sequencing data of enzymatically isolated subcutaneous adipocytes from 43 individuals plotted against BMI. *P* values were calculated using an *F*-test (with null hypothesis that slope is zero), error bars represent a confidence level of 0.95. **e**, Representative images of ex vivo differentiated human subcutaneous adipocytes predicted to have low or high hAd3 content on the basis of deconvolution of bulk RNA sequencing data. Green represents BODIPY staining, blue represents Hoechst staining. Scale bars, 100 µm. **f**, Normalized count of BODIPY-related features in ex vivo differentiated adipocytes stratified into hAd3-low and hAd3-high populations. Points represent normalized feature for cultures derived from individual subjects. $n = 8$ hAd3-low SAT, 4 hAd3-high SAT, 19 hAd3-low VAT, 4 hAd3-high VAT. **g**, UMAP projection of 39,934 mouse white adipocytes. **h**, Expression of *Adipoq* and marker genes for each mouse adipocyte subpopulation. In bar graphs, error bars represent s.e.m. and *P* values were calculated using two tailed *t*-tests with no correction for multiple comparisons.

allele, $P = 0.03$) or gluteofemoral (GFAT) (GFATadj: beta = −0.020 s.d. per allele, $P = 0.02$, Extended Data Fig. 11b) depots. We additionally stratified individuals into either 0, 1 or 2 carriers of the minor allele and observed an additive trend (G/G median VATadj −0.10 s.d., G/A median VATadj = −0.04 s.d., A/A median VATadj 0.04 s.d.; Extended Data Fig. 11c). Next, we returned to the visceral human adipocytes differentiated ex vivo, and found that samples predicted to have a higher proportion of hAd6 adipocytes were characterized by higher mitochondrial intensity and increased expression of mitochondrial and thermogenic genes (Extended Data Fig. 11d–f). Finally, our analysis of hAd6 markers suggested other pathways associated with thermogenesis, including one for 'axon guidance' (Extended Data Fig. 11g). We could not measure innervation directly using our data, because the nuclei of innervating sympathetic neurons are located in the spinal ganglia and not the fat depot itself. Nonetheless, we estimated the degree of innervation using the presence of neuron-specific gene expression in the ambient RNA of our visceral sNuc-seq samples. Indeed, the amount of pan-neuronal markers like *TUBB3* and *UCHL1*[32] strongly correlate with hAd6 proportion (Extended Data Fig. 11h), further supporting a role for hAd6 as a novel visceral adipocyte subtype with thermogenic potential.

Mouse adipocyte subpopulations

Subclustering mouse adipocytes revealed six subpopulations (Fig. 3g, h). Unlike human adipocytes, mouse adipocyte subtypes exhibit little depot enrichment (Extended Data Fig. 12a–c). There was strong diet dependency, however, as relative proportions of mAd1 and mAd3 were reduced after HFD, while the opposite was noted for mAd4 and mAd5 (Extended Data Fig. 12b, c). In contrast to the relatively good cross-species concordance between immune cells, vascular cells, and ASPCs, mouse adipocytes do not map cleanly onto human adipocyte subpopulations (Extended Data Fig. 12d–f).

As in humans, genes associated with major adipocyte functions showed some subpopulation selectivity in mice. For example, lipogenesis genes were highest in HFD-induced population mAd5 (Extended Data Fig. 12c, g). More detailed pathway analysis on mouse adipocyte subpopulations (Supplementary Table 3) showed that the chow-associated clusters mAd1–mAd3 were notably enriched in metabolic pathways, particularly those involved in lipid handling (Extended Data Fig. 12h–j). By contrast, the HFD-associated clusters mAd4–mAd6 were linked to pathways such as 'HIF-1 signalling', 'actin cytoskeleton' and 'NF-kB signalling' (Extended Data Fig. 12k–n), consistent with the known roles of hypoxia, cytoskeletal remodelling and inflammation in HFD-induced adipose dysfunction and insulin resistance[23–25].

Our data allow us to address the question of whether diet-induced changes in gene expression at the population level are shared among subpopulations or whether they reflect a change in the relative proportion of these subpopulations. To assess this, we examined the 20 most positively and negatively regulated genes from a translating ribosome affinity purification (TRAP)-based RNA-seq experiment in white adipocytes from mice fed chow or HFD[33] (Supplementary Fig. 2a). We noted that some genes (for example, *Cyp2e1* and *Fam13a*) exhibit elevated expression in chow adipocytes in almost all subpopulations, whereas for others (for example, *Cfd*), expression is largely driven by the mAd3 population which decreases in abundance with HFD (Extended Data Fig. 12b, c, Supplementary Fig. 2b). Similarly, *Sept9*, *Cdkn1a* and *Fgf13* show increased gene expression after HFD across almost all subpopulations, whereas other HFD-induced genes (for example, *Slc5a7* and *Dclk1*) increase their expression after HFD in the chow-associated clusters mAd1–mAd4 but not in the HFD-associated clusters mAd5–mAd7 (Supplementary Fig. 2b). Thus, diet-dependent expression changes reflect both alterations across all clusters and the emergence or disappearance of distinct populations.

Finally, we could not identify a mouse adipocyte population that could be clearly delineated as thermogenic. Such cells have been noted by others in WAT, even at room temperature[34]. However, when we considered the adipocytes from chow-fed mice independently, mAd1 split into three clusters (Supplementary Fig. 3a, b). Two of these clusters, mAd1B and mAd1C, were recognizable as thermogenic beige adipocytes, with relatively high expression of *Prdm16* and *Ppargc1a* in mAd1B and even higher expression of these genes, as well as expression of *Ucp1* and *Cidea* in mAd1C (Supplementary Fig. 3c). As expected, the thermogenic mAd1B and mAd1C subpopulations were enriched in ING versus PG samples (Supplementary Fig. 3d, e).

Cell–cell interactions in adipose tissue

The functions of WAT are coordinated by neural and hormonal cues from outside the fat pad[35]. There is growing appreciation, however, that intercellular communication within the depot is also critical for the WAT response to overnutrition and other stressors[36]. In particular, attention has focused on cross-talk between adipocytes and immune cells (especially macrophages) in the context of obesity[37]. To assess potential interactions between all identified cell types in different depots and at different body mass, we used CellPhoneDB[38], which uses the expression of ligand-receptor pairs as a proxy for intercellular communication (Supplementary Tables 4, 5). As expected, we detected increased potential communication between human adipocytes and macrophages in high-BMI versus low-BMI subjects; of 84 potential interactions identified between human adipocytes and macrophages, 40 (48%) were specific for high-BMI subjects, and only 3 (4%) were specific for low-BMI subjects (Fig. 4a, Extended Data Fig. 13a, d). Notably, obesity was also associated with robustly increased expression of genes encoding ligand–receptor pairs between adipocytes and many non-immune cell types, including blood and lymphatic endothelial cells, vascular SMCs, pericytes and ASPCs (Fig. 4a, b, Extended Data Fig. 13a, d). For example, out of 145 potential interactions identified between human adipocytes and endothelial cells, 65 (45%) were specific for high-BMI subjects, and only 6 (4%) were specific for low-BMI subjects (Extended Data Fig. 13d). Potential interactions between these cell types are frequently bidirectional, and receptors are often expressed on multiple cell types, suggesting networks of communication (Fig. 4b, Extended Data Fig. 13e). We also noted differential expression of ligands and receptors within human adipocyte subpopulations, lending further support to the idea that they carry out distinct functions (Extended Data Fig. 13b). The specific interactions upregulated during obesity suggest that adipocytes have a significant role in obesity-related adipose tissue remodelling. For example, adipocyte expression of angiogenic factors such as *JAG1* and *VEGFC* is increased in the obese state, as is the expression of their receptors (for example, *NOTCH3* and *KDR*) on endothelial cells, consistent with obesity-associated induction of angiogenesis by adipocytes[39] (Fig. 4b, Supplementary Table 6).

Analysis of the mouse data yielded similar results, as HFD increased the intensity of ligand–receptor pair expression, with the most prominent interactions again occurring between non-immune cell types, especially between ASPCs and adipocytes, pericytes and SMCs (Extended Data Fig. 13c). Of note, adipose niche interactions were only moderately conserved between mouse and human (Extended Data Fig. 13d). Interactions between WAT cell types include several that have been studied, such as the effect of the adipokine leptin on endothelial cells via LEPR[40], and the actions of TGF-β1 on adipose fibrosis via its receptor TGF-βR1[33]. The majority of these interactions, however, are unstudied in the context of WAT biology.

WAT cell types and human disease

Adiposity is associated with a wide range of metabolic diseases and traits, and GWAS studies have suggested a specific link between WAT and coronary artery disease, BMI-adjusted type 2 diabetes (T2D), dyslipidemia, and BMI-adjusted WHR[41–43] (a measure of body fat distribution). To determine which specific cell types in WAT are likely to mediate these associations, we used CELLECT, a method for integrating scRNA-seq and sNuc-seq data with GWAS[44]. As expected, type 1 diabetes (T1D) was significantly associated with B and T lymphocytes and NK cells, consistent with the known autoimmune basis of that disease (Fig. 4c). No WAT cell type was associated with BMI, as expected given the strong neuronal basis of body weight regulation[45]. The strongest phenotypic association for white adipocytes was with BMI-adjusted WHR, and associations approaching significance were also noted between adipocytes and high-density lipoprotein and BMI-adjusted T2D (Fig. 4c, Supplementary Table 7).

All adipocyte subpopulations were significantly associated with WHR (Fig. 4d), so we looked for genes responsible for the association with WHR that lack specificity for any particular adipocyte subpopulation. One such gene is *PPARG*, which is highly expressed in all adipocytes (Extended Data Fig. 14a). Data from the METSIM cohort indicates a strong inverse relationship between WHR and *PPARG* in whole WAT (Extended Data Fig. 14b). Unfortunately, WHR was not recorded in the cohort used to generate our floated human adipocytes. WHR is, however, highly correlated with homeostatic model assessment for insulin resistance[11] (HOMA-IR), and we found that *PPARG* expression showed a strong inverse relationship with HOMA-IR in both the METSIM cohort and in our floated adipocytes (Extended Data Fig. 14c, d). Furthermore, SNPs in the *PPARG* gene that are associated with BMI-adjusted WHR[30] are also significantly associated with *PPARG* mRNA and HOMA-IR in our floated adipocyte cohort (Extended Data Fig. 14e–h).

Adipocytes were also the cell type most likely to mediate the association of WAT with T2D, with the strongest association specifically with hAd7 (Fig. 4d). To further investigate the association between hAd7 and T2D, we plotted the abundance of hAd7 as a function of HOMA-IR in our deconvolved floated adipocyte data. This revealed that hAd7 shows significant inverse correlation with insulin resistance (Fig. 4e).

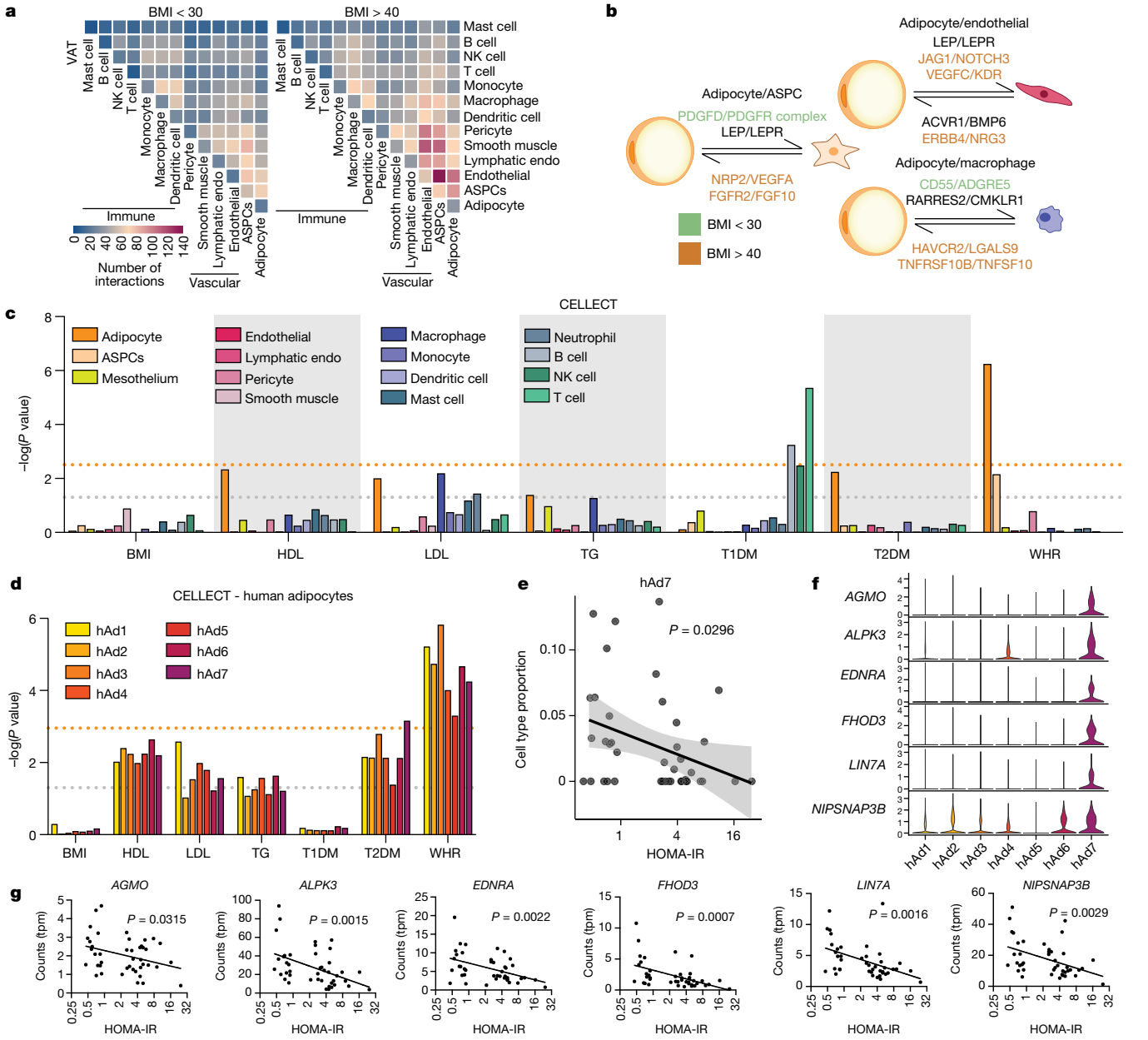

Fig. 4 | Extensive cell–cell interactions in WAT and associations with human disease traits. a, Heat map showing number of significant interactions identified between cell types in VAT of low-BMI (<30) and high-BMI (>40) individuals as determined by CellphoneDB. **b**, Selected interactions between adipocytes and ASPCs, endothelial cells, and macrophages identified using CellphoneDB; orange and green indicate interactions that are significant only with BMI > 40 and only with BMI > 30, respectively. **c**, CELLECT *P* values of the association between cell types in the human adipose sNuc-seq dataset with GWAS studies. The grey line represents $P = 0.05$ and the orange line represents significant *P* value after Bonferroni adjustment ($P = 0.003$), based on number of cell types queried. Both T2D and WHR were BMI-adjusted. TG, triglyceride. **d**, CELLECT *P* values for adipocyte subpopulations. The grey line represents $P = 0.05$ and the orange line represents significant *P* value after Bonferroni adjustment ($P = 0.001$), based on all cell subtypes queried. **e**, Estimated cell type proportion of hAd7 in bulk RNA-seq data of enzymatically isolated subcutaneous adipocytes from 43 individuals plotted against HOMA-IR. For line of best fit, $R^2 = 0.11$, the error band represents a confidence level of 0.95. **f**,**g**, Expression of hAd7 marker genes negatively correlated with HOMA-IR in human adipocyte subpopulations (**f**) and bulk RNA-sequencing data of human adipocytes (**g**). In scatter plots, *P* values were calculated using an *F*-test with the null hypothesis that the slope is zero.

We then searched for specific hAd7 marker genes that exhibit this same relationship with HOMA-IR, and identified several (Fig. 4f, g). Of note, *AGMO* (also called *TMEM195*) has emerged as a candidate locus in T2D GWAS[46,47]. Taken together, our data suggest that hAd7 may have an outsized influence on the risk of T2D, despite representing only about 1% of human adipocytes.

Additionally, although adipocytes did not meet genome-wide significance for an association with low-density lipoprotein (LDL), we found a near-significant relationship between LDL and hAd1, and to a lesser extent, hAd4 (Fig. 4c, d). Several hAd1- and hAd4-selective genes showed a strong positive relationship with LDL in our floated adipocyte cohort (Extended Data Fig. 14i, j)

We also performed CELLECT using the mouse data and noted associations between BMI-adjusted WHR and mouse adipocytes and pre-adipocytes (Extended Data Fig. 14k–m). This suggests that WHR may be determined in large part by alterations in adipocyte differentiation, a hypothesis consistent with the *PPARG* data above, and with independent studies of different WHR genes[48]. High-density lipoprotein

and triglyceride are also associated with mouse white adipocyte gene expression (Extended Data Fig. 14k–m).

Discussion

Here we present a comprehensive atlas of human and mouse WAT across depot and body mass. Our analysis reveals a rich array of cell types, including blood and lymphatic vascular cells, immune cells, and ASPCs, in addition to adipocytes. These cell types are grossly similar across species, but differ more profoundly when cellular subpopulations are explored. It is tempting to attribute these subpopulation differences to divergence across 65 million years of evolution, but other factors also need to be considered. For example, the human samples were collected after a fast, whereas the mice were collected after ad libitum feeding, which might be expected to cause some differences in cell state related to insulin signalling or related pathways.

Overall, our data highlight a central role for adipocytes in the local regulation of the adipose depot as well as in systemic physiology. The single-cell resolution of our dataset enables the identification of heterogeneity that cannot be appreciated by bulk RNA sequencing, such as a potentially visceral thermogenic subpopulation (hAd6) and a rare subpopulation associated with T2DM (hAd7). We additionally provide a framework for mouse–human comparison in studies of adipose tissue that will be an important resource for groups hoping to translate mouse findings to human treatments. These data provide a lens of unprecedented acuity that better informs our understanding of WAT biology and enables a deeper exploration of the role of adipose tissue in health and disease.

Online content

Any methods, additional references, Nature Research reporting summaries, source data, extended data, supplementary information, acknowledgements, peer review information; details of author contributions and competing interests; and statements of data and code availability are available at https://doi.org/10.1038/s41586-022-04518-2.

1. Rosen, E. D. & Spiegelman, B. M. What we talk about when we talk about fat. *Cell* **156**, 20–44 (2014).
2. Kahn, S. E., Hull, R. L. & Utzschneider, K. M. Mechanisms linking obesity to insulin resistance and type 2 diabetes. *Nature* **444**, 840–846 (2006).
3. Schwalie, P. C. et al. A stromal cell population that inhibits adipogenesis in mammalian fat depots. *Nature* **559**, 103–108 (2018).
4. Burl, R. B. et al. Deconstructing adipogenesis induced by β3-adrenergic receptor activation with single-cell expression profiling. *Cell Metab.* **28**, 300–309.e4 (2018).
5. Merrick, D. et al. Identification of a mesenchymal progenitor cell hierarchy in adipose tissue. *Science* **364**, eaav2501 (2019).
6. Hepler, C. et al. Identification of functionally distinct fibro-inflammatory and adipogenic stromal subpopulations in visceral adipose tissue of adult mice. *eLife* **7**, e39636 (2018).
7. Vijay, J. et al. Single-cell analysis of human adipose tissue identifies depot- and disease-specific cell types. *Nat. Metab.* **2**, 97–109 (2020).
8. Rajbhandari, P. et al. Single cell analysis reveals immune cell–adipocyte crosstalk regulating the transcription of thermogenic adipocytes. *eLife* **8**, e49501 (2019).
9. Sárvári, A. K. et al. Plasticity of epididymal adipose tissue in response to diet-induced obesity at single-nucleus resolution. *Cell Metab.* **33**, 437–453.e5 (2021).
10. Sun, W. et al. snRNA-seq reveals a subpopulation of adipocytes that regulates thermogenesis. *Nature* **587**, 98–102 (2020).
11. Benites-Zapata, V. A. et al. High waist-to-hip ratio levels are associated with insulin resistance markers in normal-weight women. *Diabetes Metab. Syndr. Clin. Res. Rev.* **13**, 636–642 (2019).
12. Wang, X., Park, J., Susztak, K., Zhang, N. R. & Li, M. Bulk tissue cell type deconvolution with multi-subject single-cell expression reference. *Nat. Commun.* **10**, 380 (2019).
13. Raulerson, C. K. et al. Adipose tissue gene expression associations reveal hundreds of candidate genes for cardiometabolic traits. *Am. J. Hum. Genet.* **105**, 773–787 (2019).
14. Blüher, M. Transgenic animal models for the study of adipose tissue biology. *Best Pract. Res. Clin. Endocrinol. Metab.* **19**, 605–623 (2005).
15. Rinaldi, V. D. et al. An atlas of cell types in the mouse epididymis and vas deferens. *eLife* **9**, e55474 (2020).
16. Villani, A.-C. et al. Single-cell RNA-seq reveals new types of human blood dendritic cells, monocytes, and progenitors. *Science* **356**, eaah4573 (2017).
17. Hildreth, A. D. et al. Single-cell sequencing of human white adipose tissue identifies new cell states in health and obesity. *Nat. Immunol.* **22**, 639–653 (2021).
18. Suganami, T. & Ogawa, Y. Adipose tissue macrophages: their role in adipose tissue remodeling. *J. Leukoc. Biol.* **88**, 33–39 (2010).
19. Weisberg, S. P. et al. Obesity is associated with macrophage accumulation in adipose tissue. *J. Clin. Invest.* **112**, 1796–1808 (2003).
20. Reilly, S. M. & Saltiel, A. R. Adapting to obesity with adipose tissue inflammation. *Nat. Rev. Endocrinol.* **13**, 633–643 (2017).
21. Shi, M. & Shi, G.-P. Different roles of mast cells in obesity and diabetes: lessons from experimental animals and humans. *Front. Immunol.* **3**, 7 (2012).
22. Xu, H. et al. Chronic inflammation in fat plays a crucial role in the development of obesity-related insulin resistance. *J. Clin. Invest.* **112**, 1821–1830 (2003).
23. Ferrero, R., Rainer, P. & Deplancke, B. Toward a consensus view of mammalian adipocyte stem and progenitor cell heterogeneity. *Trends Cell Biol.* **30**, 937 (2020).
24. Wang, Q. A., Tao, C., Gupta, R. K. & Scherer, P. E. Tracking adipogenesis during white adipose tissue development, expansion and regeneration. *Nat. Med.* **19**, 1338–1344 (2013).
25. Jeffery, E., Church, C. D., Holtrup, B., Colman, L. & Rodeheffer, M. S. Rapid depot-specific activation of adipocyte precursor cells at the onset of obesity. *Nat. Cell Biol.* **17**, 376–385 (2015).
26. Bäckdahl, J. et al. Spatial mapping reveals human adipocyte subpopulations with distinct sensitivities to insulin. *Cell Metab.* **33**, 1869–1882.e6 (2021).
27. Stefan, N. et al. Circulating palmitoleate strongly and independently predicts insulin sensitivity in humans. *Diabetes Care* **33**, 405–407 (2010).
28. Laber, S. et al. Discovering cellular programs of intrinsic and extrinsic drivers of metabolic traits using LipocyteProfiler. Preprint at https://doi.org/10.1101/2021.07.17.452050 (2021).
29. Rajakumari, S. et al. EBF2 determines and maintains brown adipocyte identity. *Cell Metab.* **17**, 562–574 (2013).
30. Pulit, S. L. et al. Meta-analysis of genome-wide association studies for body fat distribution in 694 649 individuals of European ancestry. *Hum. Mol. Genet.* **28**, 166–174 (2019).
31. Agrawal, S. et al. Inherited basis of visceral, abdominal subcutaneous and gluteofemoral fat depots. Preprint at https://doi.org/10.1101/2021.08.24.21262564 (2021).
32. Willows, J. W. et al. Visualization and analysis of whole depot adipose tissue neural innervation. *iScience* **24**, 103127 (2021).
33. Roh, H. C. et al. Adipocytes fail to maintain cellular identity during obesity due to reduced PPARγ activity and elevated TGFβ–SMAD signaling. *Mol. Metab.* **42**, 101086 (2020).
34. Park, J. et al. Progenitor-like characteristics in a subgroup of UCP1^{+} cells within white adipose tissue. *Dev. Cell* **56**, 985–999.e4 (2021).
35. Priest, C. & Tontonoz, P. Inter-organ cross-talk in metabolic syndrome. *Nat. Metab.* **1**, 1177–1188 (2019).
36. Schling, P. & Löffler, G. Cross talk between adipose tissue cells: impact on pathophysiology. *News Physiol. Sci.* **17**, 99–104 (2002).
37. Kane, H. & Lynch, L. Innate immune control of adipose tissue homeostasis. *Trends Immunol.* **40**, 857–872 (2019).
38. Efremova, M., Vento-Tormo, M., Teichmann, S. A. & Vento-Tormo, R. CellPhoneDB: inferring cell–cell communication from combined expression of multi-subunit ligand–receptor complexes. *Nat. Protoc.* **15**, 1484–1506 (2020).
39. Cao, Y. Angiogenesis and vascular functions in modulation of obesity, adipose metabolism, and insulin sensitivity. *Cell Metab.* **18**, 478–489 (2013).
40. Hubert, A. et al. Selective deletion of leptin signaling in endothelial cells enhances neointima formation and phenocopies the vascular effects of diet-induced obesity in mice. *Arterioscler. Thromb. Vasc. Biol.* **37**, 1683–1697 (2017).
41. Scott, R. A. et al. An expanded genome-wide association study of type 2 diabetes in Europeans. *Diabetes* **66**, 2888–2902 (2017).
42. Shungin, D. et al. New genetic loci link adipose and insulin biology to body fat distribution. *Nature* **518**, 187–196 (2015).
43. Huang, L. O. et al. Genome-wide discovery of genetic loci that uncouple excess adiposity from its comorbidities. *Nat. Metab.* **3**, 228–243 (2021).
44. Timshel, P. N., Thompson, J. J. & Pers, T. H. Genetic mapping of etiologic brain cell types for obesity. *eLife* **9**, e55851 (2020).
45. O'Rahilly, S. & Farooqi, I. S. Human obesity as a heritable disorder of the central control of energy balance. *Int. J. Obes.* **32** (Suppl. 7), S55–S61 (2008).
46. Sailer, S., Keller, M. A., Werner, E. R. & Watschinger, K. The emerging physiological role of AGMO 10 years after its gene identification. *Life* **11**, 88 (2021).
47. Dupuis, J. et al. New genetic loci implicated in fasting glucose homeostasis and their impact on type 2 diabetes risk. *Nat. Genet.* **42**, 105–116 (2010).
48. Loh, N. Y. et al. RSPO3 impacts body fat distribution and regulates adipose cell biology in vitro. *Nat. Commun.* **11**, 2797 (2020).
49. Chi, J. et al. Three-dimensional adipose tissue imaging reveals regional variation in beige fat biogenesis and PRDM16-dependent sympathetic neurite density. *Cell Metab.* **27**, 226–236.e3 (2018).
50. Katz, A. et al. Quantitative insulin sensitivity check index: a simple, accurate method for assessing insulin sensitivity in humans. *J. Clin. Endocrinol. Metab.* **85**, 2402–2410 (2000).

Methods

Collection of human adipose tissue samples

Drop-seq and floated adipocyte bulk RNA-seq. Subcutaneous adipose tissue was collected under Beth Israel Deaconess Medical Center Committee on Clinical Investigations IRB 2011P000079. Potential subjects were recruited in a consecutive fashion, as scheduling permitted, from the plastic surgery operating room rosters at Beth Israel Deaconess Medical Center. Male and female subjects over the age of 18 undergoing elective plastic surgery procedures and free of other acute medical conditions were included and provided written informed consent preoperatively. Excess adipose tissue from the surgical site was collected at the discretion of the surgeon during the normal course of the procedure. Subjects with a diagnosis of diabetes, or taking insulin-sensitizing medications such as thiazolidinediones or metformin, chromatin-modifying enzymes such as valproic acid, anti-retroviral medications, or drugs known to induce insulin resistance such as mTOR inhibitors or systemic steroid medications, were excluded.

sNuc-Seq. Subcutaneous and visceral adipose tissue was collected under BIDMC Committee on Clinical Investigations IRB 2011P000079 and University of Pittsburgh Medical Center STUDY 19010309. At BIDMC, potential subjects were recruited in a consecutive fashion, as scheduling permitted, from the gynecological, vascular, and general surgery rosters. Male and female subjects over the age of 18 undergoing plastic surgery (panniculectomy, thighplasty or deep inferior epigastric perforators), gynecological surgery (total abdominal hysterectomy and bilateral salpingo-oophorectomy) or general surgery (cholecystectomy (CCY) or colon polyp surgery) and free of other acute medical conditions were included and provided written informed consent preoperatively. Excess adipose tissue from the surgical site was collected at the discretion of the surgeon during the normal course of the procedure. The exclusion criteria were any subjects taking thiazolidinediones, chromatin-modifying enzymes such as valproic acid, anti-retroviral medications, and drugs known to induce insulin resistance such as mTOR inhibitors or systemic steroid medications. At UPMC, inclusion criteria were patients receiving bariatric surgery (vertical sleeve gastrectomy or roux en Y gastric bypass) or lean controls (hernia or CCY surgeries) ages 21–60, exclusion criteria were diagnosis of diabetes (Type 1 or Type 2), pregnancy, alcohol or drug addiction, bleeding or clotting abnormality, or inflammatory abdominal disease. All patients provided written informed consent preoperatively. Excess adipose tissue from the surgical site was collected at the discretion of the surgeon during the normal course of the procedure. 200–500 mg samples were flash frozen immediately after collection for downstream processing.

Mouse adipose tissue samples

All animal experiments were performed under a protocol approved by the BIDMC Institutional Animal Care and Use Committee. Male C57Bl/6J 16-week-old HFD-fed (JAX 380050) and chow-fed (JAX 380056) mice were obtained from The Jackson Laboratory and maintained on 60% HFD (Research Diets, D12492) or chow diet (8664 Harlan Teklad, 6.4% wt/wt fat), respectively, for three weeks before sacrifice at 19 weeks. Female 6-week-old chow fed C57Bl/6J mice (JAX 380056) were maintained on 60% HFD for 13 weeks before sacrifice at 19 weeks. Mice were maintained under a 12 h light/12 h dark cycle at constant temperature (23 °C) and humidity in the range of 30%–70% with free access to food and water. There were no calculations performed to determine sample size. Animals were not randomized and researchers were not blinded to the diet of the animal due to the nature of the study. During dissection, to avoid contamination by cells from the inguinal lymph node, we excised the node with a fairly wide margin, possibly de-enriching beige adipocytes from our samples[49].

Mature human adipocyte sample preparation

Purification of mature human adipocytes. Whole tissue subcutaneous adipose specimens were freshly collected from the operating room. Skin was removed, and adipose tissue was cut into 1- to 2-inch pieces and rinsed thoroughly with 37 °C PBS to remove blood. Cleaned adipose tissue pieces were quickly minced in an electric grinder with 3/16-inch hole plate, and 400 ml of sample was placed in a 2-liter wide-mouthed Erlenmeyer culture flask with 100 ml of freshly prepared blendzyme (Roche Liberase TM, research grade, cat. no. 05401127001, in PBS, at a ratio of 6.25 mg per 50 ml) and shaken in a 37 °C shaking incubator at 120 r.p.m. for 15–20 min to digest until the sample appeared uniform. Digestion was stopped with 100 ml of freshly made KRB (5.5 mM glucose, 137 mM NaCl, 15 mM HEPES, 5 mM KCl, 1.25 mM $CaCl_2$, 0.44 mM KH_2PO_4, 0.34 mM Na_2HPO_4 and 0.8 mM $MgSO_4$), supplemented with 2% BSA. Digested tissue was filtered through a 300 μM sieve and washed with KRB/albumin and flow through until only connective tissue remained. Samples were centrifuged at 233*g* for 5 min at room temperature, clear lipid was later removed, and floated adipocyte supernatant was collected, divided into aliquots and flash-frozen in liquid nitrogen.

Sample selection and Bulk-RNA-seq library construction. Fasting serum was collected and insulin, glucose, free fatty acids, and a lipid panel were measured by Labcorp. BMI measures were derived from electronic medical records and confirmed by self-reporting, and measures of insulin resistance, the homeostasis model assessment-estimated insulin resistance index (HOMA-IR) and revised quantitative insulin sensitivity check index (QUICKI) were calculated[50,51]. Female subjects in the first and fourth quartiles for either HOMA-IR or QUICKI and matched for age and BMI were processed for RNA-seq.

Total RNA from about 400 μl of thawed floated adipocytes was isolated in TRIzol reagent (Invitrogen) according to the manufacturer's instructions. For RNA-seq library construction, mRNA was purified from 100 ng of total RNA by using a Ribo-Zero rRNA removal kit (Epicentre) to deplete ribosomal RNA and convert into double-stranded complementary DNA by using an NEBNext mRNA Second Strand Synthesis Module (E6111L). cDNA was subsequently tagmented and amplified for 12 cycles by using a Nextera XT DNA Library Preparation Kit (Illumina FC-131). Sequencing libraries were analysed with Qubit and Agilent Bioanalyzer, pooled at a final loading concentration of 1.8 pM and sequenced on a NextSeq500.

Single-cell and single-nucleus sample preparation and processing

SVF isolation and Drop-seq. Adipose tissue samples were collected and processed as above. After removal of floated adipocytes, remaining supernatant was aspirated and the remaining pelleted stromal vascular fraction (SVF)was combined from multiple tubes. The combined SVF was washed 2 times with 50 ml cold PBS with 233*g* for 5 min centrifugation between washes. Erythrocytes were depleted with two rounds of 25 ml. ACK lysing buffer (Gibco A1049201) exposure (5 min at RT followed by 233*g* × 5 min centrifugation). Remaining SVF pellet was further washed two times with 50 ml cold PBS prior to counting on a haematocytometer and loading onto Drop-seq microfluidic devices. Drop-seq was performed as described[52], with the following modifications: first, flow rates of 2.1 ml h^{-1} were used for each aqueous suspension and 12 ml h^{-1} for the oil. Second, libraries were sequenced on the Illumina NextSeq500, using between 1.6–1.7 pM in a volume of 1.2 ml HT1 and 3 ml of 0.3 μM Read1CustSeqB (GCCTGTCCGCGGAAGCAGTGGTATCAACGCAGAGTAC) using a 20 × 8 × 60 read structure.

sNuc-seq. Nuclei were isolated from frozen mouse and human adipose tissue samples for 10x snRNA-seq using a slightly modified approach to what was previously described[53–55]. Samples were kept frozen on dry ice until immediately before nuclei isolation, and all sample handling

steps were performed on ice. Each flash-frozen adipose tissue sample was placed into a gentleMACS C tube (Miltenyi Biotec) with 2 ml freshly prepared TST buffer (0.03% Tween 20 (Bio-Rad), 0.01% Molecular Grade BSA (New England Biolabs), 146 mM NaCl (ThermoFisher Scientific), 1 mM $CaCl_2$ (VWR International), 21 mM $MgCl_2$ (Sigma Aldrich), and 10 mM Tris-Hcl pH 7.5 (ThermoFisher Scientific) in Ultrapure water (ThermoFisher Scientific)) with or without 0.2 U μl^{-1} of Protector RNase Inhibitor (Sigma Aldrich). gentleMACS C tubes were then placed on the gentleMACS Dissociator (Miltenyi Biotec) and tissue was dissociated by running the program mr_adipose_01 twice, and then incubated on ice for 10 min. Lysate was passed through a 40 µm nylon filter (CellTreat) and collected into a 50 ml conical tube (Corning). Filter was rinsed with 3 ml of freshly prepared ST buffer buffer (146 mM NaCl, 1 mM $CaCl_2$, 21 mM $MgCl_2$; 10 mM Tris-Hcl pH 7.5) with or without 0.2 U μl^{-1} RNase Inhibitor, and collected into the same tube. Flow-through was centrifuged at 500*g* for 5 min at 4 °C with brake set to low. Following centrifugation, supernatant was removed, and the nuclear pellet was resuspended in 50–200 µl PBS pH 7.4 (ThermoFisher Scientific) with 0.02% BSA, with or without 0.2 U μl^{-1} RNase inhibitor. In order to reduce ambient mRNA, the nuclear pellets of some samples were washed 1–3 times with 5 ml PBS, 0.02% BSA before final resuspension. An aliquot of nuclei from each sample was stained with NucBlue (Thermofisher Scientific), counted in a haemocytometer using fluorescence to identify intact nuclei, and then immediately loaded on the 10x Chromium controller (10x Genomics) according to the manufacturer's protocol.

For each sample, 10,000–16,500 nuclei were loaded in one channel of a Chromium Chip (10x Genomics). The Single Cell 3′ v3.1 chemistry was used to process all samples. cDNA and gene expression libraries were generated according to the manufacturer's instructions (10x Genomics). cDNA and gene expression library fragment sizes were assessed with a DNA High Sensitivity Bioanalyzer Chip (Agilent). cDNA and gene expression libraries were quantified using the Qubit dsDNA High Sensitivity assay kit (ThermoFisher Scientific). Gene expression libraries were multiplexed and sequenced on the Nextseq 500 (Illumina) with a 75-cycle kit and the following read structure: Read 1: 28 cycles, Read 2: 55 cycles, Index Read 1: 8 cycles.

Public datasets

Publicly available datasets and databases used were the following: METSIM RNA-seq data from Raulerson et al.[13] (GSE135134); single-cell ASPC data from Burl et al.[4] (SRP145475), Hepler et al.[6] (GSE111588), Merrick et al.[5] (GSE128889), Sárvári et al.[9] (GSE160729), and Schwalie et al.[3] (E-MTAB-6677); human assembly GRCh38 and GENCODE annotation 27 (https://www.gencodegenes.org/human/release_27.html); mouse assembly GRCm38 and GENCODE annotation M16 (https://www.gencodegenes.org/mouse/release_M16.html).

Sequencing, read alignments, and quality control

Single-cell and single-nucleus RNA-seq data analysis. Raw sequencing reads were demultiplexed to FASTQ format files using bcl2fastq (Illumina; version 2.20.0). Digital expression matrices were generated from the FASTQ files using the Drop-Seq tools (https://github.com/broadinstitute/Drop-seq, version 2.4.0) pipeline, with appropriate adjustments made to the default program parameters to account for the different read-structures in the scRNA Drop-Seq data and sNuc 10x data. Reads from mouse and human were aligned with STAR[56] (version 2.7.3) against the GRCm38 and GRCh38 genome assemblies, respectively. Gene counts were obtained, on a per-droplet basis, by summarizing the unique read alignments across exons and introns in appropriate GENCODE annotations (release 16 of the mouse annotation and release 27 of the human annotation). In order to adjust for downstream effects of ambient RNA expression within mouse nuclei (hereafter "cells"), we used CellBender[57] (version 0.2.0) to remove counts due to ambient RNA molecules from the count matrices and estimate the true cells. We also used CellBender to distinguish droplets containing cells from droplets containing only ambient RNA, by selecting droplets with >50% posterior probability of containing a cell. We compared the true cell estimation obtained using CellBender against the same using the DropletUtils software package[58], which estimates ambient RNA expression but does not remove any ambient counts, keeping only the cells that were marked as not ambient by both algorithms. To address ambient RNA in the human sNuc data, we calculated spliced and unspliced RNA content in each cell, because nuclei have a high unspliced RNA content, a high percentage of spliced RNA indicates a high ambient RNA content. We therefore removed sNuc-seq cells containing over 75% spliced RNA. All samples were assessed for doublet content using scrublet[59] version 0.2.1, and cells called as doublets were removed before further analysis. All cells were further filtered to have greater than 400 unique molecular identifiers (UMIs) with <10% of UMIs from mitochondrial genes. Genes were filtered such that only genes detected in two or more cells were retained. For the human data, the median number of UMIs detected per cell was 2,559 and the median number of genes detected per cell was 1,524. For the mouse data, the median number of UMIs detected per cell was 2,291 and the median number of genes detected per cell was 1,369.

Bulk RNA-seq analysis. Raw sequencing reads were demultiplexed by using bcl2fastq (Illumina). Salmon[60] (version 1.1.0) was used to simultaneously map and quantify transcript abundances of hg19 genes annotated by release 19 of the GENCODE project's human reference. Salmon was run using "full" selective alignment (SAF) with mapping validation as described previously[61]. Gene counts were summarized from transcript abundances using the tximport package for R[62].

Integration, clustering, subclustering and annotation

Integration, clustering and subclustering analysis were performed using Seurat 4.0.0[63]. The gene counts were normalized using SCTransform[64], and regressed on mitochondrial read percentage, ribosomal read percentage, and cell cycle score as determined by Seurat. In order to avoid smoothing over depot differences, for integration human and mouse data were grouped by 'individual', that is, if both subcutaneous and visceral adipose tissue for an individual human or mouse were available, they were pooled together during this step. Individuals were integrated with reciprocal principal components analysis (PCA), using individuals that had both subcutaneous and visceral samples as references. As a result, the human and mouse references were comprised exclusively from the sNuc-seq cohort. To integrate, references were integrated together, then the remaining samples— sNuc-seq individuals with only subcutaneous data as well as all Drop-seq samples—were mapped to the reference. For clustering, 5,000 variable genes were used, and ribosomal and mitochondrial genes were removed from the variable gene set before running PCA and calculating clusters using a Louvain algorithm, 40 principal components, and a resolution of 0.5. Clusters were identified as adipocytes, preadipocytes, mesothelial cells, vascular cells, or immune cells using marker genes, subset into individual objects, and re-integrated using the above method. Samples with fewer than 50 cells in the subset were removed before re-integration. This led to samples having artificially fewer cells in some instances—for example some Drop-seq samples had cells that clustered with adipocytes, but these cells were removed in subclustering because the small numbers of cells introduced too much variability into the integration. Subclustering was performed using a range of variable genes (1,000–2,000), PCs (10–40) and resolutions (0.2–0.6). Markers were calculated using a non-parametric Wilcoxon rank sum test with *P* values adjusted using Bonferroni correction (Supplementary Tables 1, 2), and clusters were evaluated based on the distinctness of called markers to determine the final subclustering conditions. In the subclustered objects, we removed clusters that appeared to represent doublets based on the score assigned by scrublet[59], or that appeared to be driven by high ambient RNA content as determined by percentage of mitochondrial genes and spliced/unspliced RNA

ratio. The remaining clusters were annotated based on marker gene expression. In some cases, smaller subclusters (T and NK cells, B cells, monocytes/neutrophils) were further subset and PCA and clustering analysis but not integration was re-run in order to assign clusters. After subcluster annotation, identities were mapped back onto the original object and cells that were removed from the subclustered objects were similarly removed from the all-cell object.

Deconvolution of bulk RNA-seq data

Bulk RNA sequencing data for subcutaneous adipose tissue from the METSIM cohort were obtained as described previously[13]. Only individuals with available metabolic phenotyping data were used for the deconvolution analysis. Bulk RNA sequencing data for floated human adipocytes were obtained described above. Deconvolution analysis was performed using MuSiC[12] (version 0.1.1) with human sNuc subcutaneous all cell or adipocyte data as reference. Marker genes used for deconvolution can be found in Supplementary Table 1.

Comparison between mouse and human datasets

Mapping of mouse cells onto human clusters was performed using Seurat multimodal reference mapping[65]. To run, for the all-cell and each subset, the mouse data were prepared by extracting the counts matrix from the mouse sNuc object and mapping the mouse gene names to their human orthologs using a database of ortholog mappings from Mouse Genome Informatics (http://www.informatics.jax.org/homology.shtml). In the case of multi-mapping, the first ortholog pair was used. The mouse object was then split by sample and mapped onto the sNuc-seq data from the matching human all-cell or subset object using the RNA assay and PCA reduction.

Integration of ASPCs from this and other studies

Data was obtained from Burl et al.[4] (SRP145475), Hepler et al.[6] (GSE111588), Merrick et al.[5] (GSE128889), Sárvári et al.[9] (GSE160729), and Schwalie et al.[3] (E-MTAB-6677); processed data, metadata, and/or cell type designations were obtained from the authors when necessary. Datasets were subset to contain only ASPCs, grouped by individual animal or experiment when possible or by laboratory when not, and integrated with the data from this paper (grouped by animal) using RPCA integration without references with 1,500 variable genes. The UMAP reduction was calculated using the top 20 PCs and ASPCs were grouped by cell type annotations from their original papers for analysis.

Immunohistochemistry

Subcutaneous (abdominal) and omental adipose tissue biopsies belonging to lean and obese women (GRIA4: subcutaneous, 5 lean and 5 obese individuals; PGAP1: subcutaneous, 5 lean, 4 obese, visceral 3 lean, 4 obese; EBF2: omental, 3 lean and 4 obese individuals; AGMO: subcutaneous, 4 lean and 4 obese individuals, for all experiments two slides per individual for GRIA4, EBF2, AGMO, one slide per individual for PGAP1) were fixed (overnight in 4% paraformaldehyde at 4 °C, dehydrated, paraffin embedded and sectioned (4 µm thick). The following primary antibodies and respective dilution were used: GRIA4, 1:200, 23350-1-AP, Proteintech; PGAP1, 1:400, Cat. #55392-1-AP, Proteintech EBF2, 1:1000, AF7006, R&D systems; AGMO (TMEM195) 1:100, orb395684, Biorbyt. In brief, after rinsing in PBS, tissue slices were blocked with 3% normal goat serum and incubated with the primary antibody in PBS, overnight at 4 °C. After a thorough rinse in PBS, sections were incubated in 1:200 v/v biotinylated secondary antibody solution for 30 min (Invitrogen), rinsed in PBS and incubated in avidin-biotin-peroxidase complex (ABC Standard, Vector Laboratories), washed several times in PBS and lastly incubated in 3,3′-diaminobenzidine tetrahydrochloride (0.05% in 0.05 M Tris with 0.03% H_2O_2; 5 min). After immunohistochemical staining, sections were counterstained with hematoxylin, dehydrated in ethanol, cleared in xylene and covered with coverslip using Eukitt (Merck). All observations were performed using Nikon Eclipse E800 light microscope.

Immunofluorescence microscopy of mature human adipocytes

Adipocyte immunofluorescence protocol was adapted from Sárvári et al[9]. Abdominal subcutaneous adipose tissue was collected from two adult female human subjects (BMI 24.9 and 40.3) as above and placed on ice. Tissue was minced and digested with 1 mg ml^{-1} type II collagenase (Sigma-Aldrich, C6885) in Hanks' balanced salt solution supplemented with 0.5% fatty acid-free BSA (Sigma-Aldrich, A6003) at 37° in a water bath with constant shaking at 250 rpm. The cell suspension was filtered through a 250 µM nylon mesh strainer (Thermo, 87791) and washed three times with Krebs–Ringer bicarbonate buffer containing 1% fatty acid-free BSA. All washes throughout this protocol were performed without centrifugation to minimize adipocyte damage and loss; cell suspension was maintained upright for at least 5 min to allow mature adipocytes to float, and infranatant was removed with a needle and syringe. The floating adipocytes were fixed with 2% PFA and 1% sucrose in PBS for 30 min with constant rotation followed by three washes with 2% fatty acid-free BSA in PBS. Adipocytes were subsequently permeabilized with 0.5% Triton-X (Thermo, 28314) in PBS for five minutes, and incubated with 2.5 µg ml^{-1} trypsin (Corning, 25053CI) in PBS for 10 min at 37° in a water bath with constant shaking. Adipocytes were then blocked with 2% fatty acid-free BSA in PBS for 30 min, and incubated overnight at room temperature with rabbit polyclonal anti-GRIA4 (Proteintech, 23350-1-AP) diluted 1:100 in 500 µl 2% fatty acid-free BSA in PBS with constant rotation. The adipocytes were then washed twice for 10 min each with 0.1% fatty acid-free BSA and 0.05% Tween-20 (Sigma-Aldrich, P9416) in PBS, followed by incubation with goat anti-rabbit Alexa Fluor 546 (Thermo, A-11035) secondary antibody diluted 1:500 in 2% fatty acid-free BSA for 2 h with rotation. For the final 30 min of incubation, Hoechst 33342 (Thermo, 62249) and BODIPY 493/503 (Invitrogen, D3922) were added at 1:500 dilutions. Adipocytes were washed twice and resuspended in 300 µl Fluoromount G (Southern Biotech, 0100-01) and mounted on glass slides with 1.4–1.6 mm concavity wells (Electron Microscopy Sciences, 71878-03). A sample of adipocytes was also incubated as above but without primary antibody to verify the specificity of the secondary antibody. Fluorescence images were acquired using Zeiss LSM 880 Upright Laser Scanning Confocal Microscope with filter cubes for DAPI, GFP, and Rhodamine in parallel using the 20× objective and processed using Zen Black 2.3 software. Images were analysed and counted with ImageJ v. 1.53 k.

Ex vivo differentiation and transcriptional and high-content image-based characterization of differentiating primary human adipocyte progenitors

We obtained adipocyte progenitors from subcutaneous and visceral adipose tissue from patients undergoing a range of abdominal laparoscopic surgeries (sleeve gastrectomy, fundoplication or appendectomy). The visceral adipose tissue is derived from the proximity of the angle of His and subcutaneous adipose tissue obtained from beneath the skin at the site of surgical incision. Additionally, human liposuction material was obtained. Each participant gave written informed consent before inclusion and the study protocol was approved by the ethics committee of the Technical University of Munich (study no. 5716/13). Isolation of AMSCs was performed as previously described[28], and cells were differentiated in culture over 14 days. Ex vivo differentiated adipocytes were stained and imaged, and features were extracted using LipocyteProfiler as described[28]. RNA-sequencing libraries were prepared and sequenced and QC'ed as previously described[28]. Bulk-RNA sequencing counts from subcutaneous and visceral samples differentiated for 14 days were deconvoluted using both subcutaneous and visceral adipocytes as reference as described above. Raw images collected during LipocyteProfiler analysis were randomly selected from samples predicted to have high or low content of hAd3, hAd5, or hAd6 adipocytes, and pseudocoloured and combined using Adobe Photoshop.

Gene pathway analysis

Analysis of enriched pathways in adipocyte markers was performed using clusterProfiler[66] (version 3.16.1). Adipocyte cluster markers were filtered to a Benjamini–Hochberg adjusted *P*-value < .05, then evaluated for enrichment in GO biological pathways or KEGG pathways containing under 300 genes. All pathways and *P* values can be found in Supplementary Table 3.

Identification and analysis of EBF2 SNP association with visceral adiposity

VAT, ASAT, and GFAT volumes in 40,032 individuals from the UK Biobank[67,68] who underwent MRI imaging were quantified as described elsewhere[69]. Variant rs4872393 was identified as a lead SNP associated with VATadj and waist-to-hip ratio from summary statistics of two prior studies[31,70]. Among the cohort who underwent MRI imaging, all variants at this locus (±250 kb around rs4872393) with minor allele frequency ≥ 0.005 and imputation quality (INFO) score ≥ 0.3 were analysed. For all 554 nominally significant ($P < 0.05$) variants associated with VATadj in this region, a secondary conditional analysis testing for association with VATadj was performed controlling for rs4872393 carrier status ($P < 0.05/554 = 9 \times 10^{-5}$). Participants were excluded from analysis if they met any of the following criteria: (1) mismatch between self-reported sex and sex chromosome count, (2) sex chromosome aneuploidy, (3) genotyping call rate < 0.95, or (4) were outliers for heterozygosity. Up to 37,641 participants were available for analysis. Fat depot volumes adjusted for BMI and height ('adj' traits) were calculated by taking the residuals of the fat depot in sex-specific linear regressions against age at the time of MRI, age squared, BMI, and height[31]. Each trait was scaled to mean 0 and variance 1 in sex-specific groups before being combined for analysis. Linear regressions between a given trait-variant pair were adjusted for age at the time of imaging, age squared, sex, the first 10 principal components of genetic ancestry, genotyping array, and MRI imaging center. Analyses were performed using R 3.6.0 (R Project for Statistical Computing). *EBF2* regional visualization plot was made with the LocusZoom online tool[71].

Calculation of pseudobulk datasets to estimate adipose innervation

Approximate bulk RNA-seq datasets (pseudobulk) were obtained for visceral sNuc-seq samples by summing the total expression per-gene across all droplets containing a valid 10x cell barcode. This includes all cells that would normally have been removed in the single-nuclei studies by any of the filtering criteria (above): doublet score, splicing content, droplets with fewer than 400 UMIs, etc, in order to preserve the ambient RNA present in otherwise empty droplets. Repeated UMIs were still collapsed into single counts (per-droplet) before summing. Amounts of pan-neuronal markers were calculated using this pesudobulk dataset and plotted against the proportion of visceral populations hAd2 and hAd6 relative to total adipocytes in each sample.

Prediction of cell–cell interactions

Analysis of cell–cell interactions was performed using CellphoneDB[38] (version 2.0.0). For human data, sNuc-seq count data were split into files containing cells from subcutaneous and visceral fat from individuals with BMI lower than 30 or higher than 40. CellphoneDB with statistical analysis was run on each file separately to evaluate interactions in each condition. For mouse data, count data were split into files containing cells from the inguinal and perigonadal fat of chow- and HFD-fed mice. Mouse gene names were converted to human gene names, as above, before running CellphoneDB with statistical analysis on each file.

Identification of candidate aetiologic cell types using CELLEX and CELLECT

CELLECT and CELLEX were used to identify candidate aetiological cell types for a total of 23 traits. The input data for CELLECT is GWAS summary statistics for a given trait and cell type expression specificity (ES) estimates derived from single-cell RNA-seq data. The output is a list of prioritized candidate aetiologic cell types for a given trait. ES estimates were calculated using CELLEX (version 1.1), which computes robust estimates of ES by relying on multiple expression specificity measures (for further details see Timshel et al.[44]). CELLEX was run separately on the raw mouse and human (sNuc) gene expression matricies to compute gene expression specificities for each cluster based on the clustering assignment reported above. The resulting cell type specificity matrix was used along with multiple GWAS studies[30,72–76] (Extended Data Table 3) as input for CELLECT[44] (version 1.1), which was run with default parameters. Significant cell types were identified using a by-trait and by-species Bonferroni *P*-value threshold of $P < 0.05$.

SNP analysis for bulk mRNA-seq cohort

The raw GTC SNP expression data from Infinium OmniExpress-24 Kit was converted to VCF format using Picard version 2.21.6. The pre-processing of the SNP data before phasing and imputation was performed using plink2 (https://www.cog-genomics.org/plink/2.0/). The SNP genotype was then phased and imputed using the Eagle v2.3.5[77] and Minimac3[78] packages, respectively. SNPs were mapped to the NCBI database using the rsnps package (https://CRAN.R-project.org/package=rsnps) and filtered to keep only SNPs that had a minor allele frequency > 0.05. For plotting gene expression against genotype, bulk RNA sequencing data were TMM normalized using edgeR[79]. Statistical validation for significance was done using the Wilcoxon rank-sum test, which is a non-parametric test assuming independent samples.

Statistics

P-values for scatterplots were calculated using GraphPad Prism version 8.0 and represent the results of an extra sum-of-squares *F*-test with the null hypothesis that the slope equals zero. All error bars on bar graphs represent standard error. Statistics on proportional composition graphs were calculated using scCODA[80] (version 0.1.2) using the Hamiltonian Monte Carlo sampling method. The model formula used was 'Depot + BMI' (human) or 'Depot + Diet') (mouse) for all objects in for which both of these covariates were present, or the individual covariate when only a single condition was present.

Reporting summary

Further information on research design is available in the Nature Research Reporting Summary linked to this paper.

Data availability

Single-cell RNA expression and count data are deposited in the Single Cell Portal (study no. SCP1376). Processed count data for bulk RNA-seq and differential gene expression matrices for single-cell and single-nucleus RNA-seq have been deposited in the Gene Expression Omnibus (bulk-sequencing accession GSE174475, scRNA-seq accession GSE176067, sNuc-seq accession GSE176171); raw sequencing reads for mouse data are available in the Sequence Read Archive under study no. SRP322736. FASTQ and SNP array files for human samples are deposited in dbGaP under accession phs002766.v1.p1. Source data are provided with this paper.

Code availability

Data analysis pipelines used in this study for processing of raw sequencing data, integration and clustering can be obtained from https://gitlab.com/rosen-lab/white-adipose-atlas.

51. Matthews, D. R. et al. Homeostasis model assessment: insulin resistance and β-cell function from fasting plasma glucose and insulin concentrations in man. *Diabetologia* **28**, 412–419 (1985).

52. Macosko, E. Z. et al. Highly parallel genome-wide expression profiling of individual cells using nanoliter droplets. *Cell* **161**, 1202–1214 (2015).
53. Drokhlyansky, E. et al. The human and mouse enteric nervous system at single-cell resolution. *Cell* **182**, 1606–1622.e23 (2020).
54. Slyper, M. et al. A single-cell and single-nucleus RNA-seq toolbox for fresh and frozen human tumors. *Nat. Med.* **26**, 792–802 (2020).
55. Delorey, T. M. et al. A single-cell and spatial atlas of autopsy tissues reveals pathology and cellular targets of SARS-CoV-2. Preprint at https://doi.org/10.1101/2021.02.25.430130 (2021).
56. Dobin, A. et al. STAR: ultrafast universal RNA-seq aligner. *Bioinformatics* **29**, 15–21 (2013).
57. CellBender remove-background: a deep generative model for unsupervised removal of background noise from scRNA-seq datasets. Preprint at https://doi.org/10.1101/791699 (2019).
58. Lun, A. T. L. et al. EmptyDrops: distinguishing cells from empty droplets in droplet-based single-cell RNA sequencing data. *Genome Biol.* **20**, 63 (2019).
59. Wolock, S. L., Lopez, R. & Klein, A. M. Scrublet: computational identification of cell doublets in single-cell transcriptomic data. *Cell Syst.* **8**, 281–291.e9 (2019).
60. Patro, R., Duggal, G., Love, M. I., Irizarry, R. A. & Kingsford, C. Salmon provides fast and bias-aware quantification of transcript expression. *Nat. Methods* **14**, 417–419 (2017).
61. Srivastava, A. et al. Alignment and mapping methodology influence transcript abundance estimation. *Genome Biol.* **21**, 239 (2020).
62. Soneson, C., Love, M. I. & Robinson, M. D. Differential analyses for RNA-seq: transcript-level estimates improve gene-level inferences. *F1000Research* **4**, 1521 (2015).
63. Stuart, T. et al. Comprehensive integration of single-cell data. *Cell* **177**, 1888–1902.e21 (2019).
64. Hafemeister, C. & Satija, R. Normalization and variance stabilization of single-cell RNA-seq data using regularized negative binomial regression. *Genome Biol.* **20**, 296 (2019).
65. Hao, Y. et al. Integrated analysis of multimodal single-cell data. *Cell* **184**, 3573–3587.e29 (2021).
66. Yu, G., Wang, L.-G., Han, Y. & He, Q.-Y. clusterProfiler: an R package for comparing biological themes among gene clusters. *OMICS J. Integr. Biol.* **16**, 284–287 (2012).
67. Littlejohns, T. J. et al. The UK Biobank imaging enhancement of 100,000 participants: rationale, data collection, management and future directions. *Nat. Commun.* **11**, 2624 (2020).
68. Sudlow, C. et al. UK Biobank: an open access resource for identifying the causes of a wide range of complex diseases of middle and old age. *PLoS Med.* **12**, e1001779 (2015).
69. Agrawal, S. et al. Association of machine learning-derived measures of body fat distribution in >40,000 individuals with cardiometabolic diseases. Preprint at https://doi.org/10.1101/2021.05.07.21256854 (2021).
70. Kichaev, G. et al. Leveraging polygenic functional enrichment to improve GWAS power. *Am. J. Hum. Genet.* **104**, 65–75 (2019).
71. Pruim, R. J. et al. LocusZoom: regional visualization of genome-wide association scan results. *Bioinformatics* **26**, 2336–2337 (2010).
72. Mahajan, A. et al. Fine-mapping type 2 diabetes loci to single-variant resolution using high-density imputation and islet-specific epigenome maps. *Nat. Genet.* **50**, 1505–1513 (2018).
73. Loh, P.-R., Kichaev, G., Gazal, S., Schoech, A. P. & Price, A. L. Mixed-model association for biobank-scale datasets. *Nat. Genet.* **50**, 906–908 (2018).
74. Finucane, H. K. et al. Partitioning heritability by functional annotation using genome-wide association summary statistics. *Nat. Genet.* **47**, 1228–1235 (2015).
75. Teslovich, T. M. et al. Biological, clinical and population relevance of 95 loci for blood lipids. *Nature* **466**, 707–713 (2010).
76. Bradfield, J. P. et al. A genome-wide meta-analysis of six type 1 diabetes cohorts identifies multiple associated loci. *PLoS Genet.* **7**, e1002293 (2011).
77. Loh, P.-R. et al. Reference-based phasing using the Haplotype Reference Consortium panel. *Nat. Genet.* **48**, 1443–1448 (2016).
78. Das, S. et al. Next-generation genotype imputation service and methods. *Nat. Genet.* **48**, 1284–1287 (2016).
79. Robinson, M. D., McCarthy, D. J. & Smyth, G. K. edgeR: a Bioconductor package for differential expression analysis of digital gene expression data. *Bioinformatics* **26**, 139–140 (2010).
80. Büttner, M., Ostner, J., Müller, C., Theis, F. & Schubert, B. scCODA: a Bayesian model for compositional single-cell data analysis. *Nat. Commun.* **12**, 6876 (2021).

Acknowledgements This work was supported by NIH grants RC2 DK116691 to E.D.R., L.T.T., A.C., O.A. and A.R., AHA POST14540015 and DoD PRMRP-DAW81XWH to L.T.T., Broad-BADERC Collaboration Initiative Award (NIH 5P30DK057521) to L.T.T. and E.D.R., and R01 DK102173 to E.D.R. M.P.E. is supported by NIH grant F32DK124914. Additional support includes PRIN 2017 (Italian Ministry of University, no. 2017L8Z2EM) to A. Giordano, T.H.P. acknowledges the Novo Nordisk Foundation (unconditional donation to the Novo Nordisk Foundation Center for Basic Metabolic Research; grant number NNF18CC0034900) and the Lundbeck Foundation (grant number R190-2014-3904), grants AMP-T2D RFB8b (FNIH) and UM1DK126185 (NIDDK) to M.C., Sarnoff Cardiovascular Research Foundation Fellowship to S.A., grants 1K08HG010155 and 1U01HG011719 to A.V.K. from the National Human Genome Research Institute, and a sponsored research agreement from IBM Research to the Broad Institute of MIT and Harvard to A.V.K. All single cell library construction and sequencing was performed through the Boston Nutrition Obesity Research Center Functional Genomics and Bioinformatics Core (NIH P30DK046200). We thank C. Usher for artistic support and M. Udler for helpful discussions.

Author contributions M.P.E., L.T.T. and E.D.R. conceived of the project. M.P.E. and E.D.R. wrote the manuscript with assistance from L.T.T., C.J., O.A. and A.R. M.P.E., A.L.E., D.P., D.T., G.C., A.D.V., A.S., E. McGonagle, S.S., S.L., G.P.W., M.L.V., A. Gulko and E. Merkel performed experiments. G.P.W., A. Gulko, Z.K., E.D.F., J.D., C.G.B., W.G., A.C., S.J.L., B.T.L., D.M. and A.T. collected samples. M.P.E., C.J., A.M.J., H.D., S.A., A.K. and H.S. performed computational analysis. A.V.K., M.C., T.H.P., A. Giordano, O.A. and A.R. provided additional intellectual input.

Competing interests S.A. has served as a scientific consultant to Third Rock Ventures. A.V.K. has served as a scientific advisor to Sanofi, Amgen, Maze Therapeutics, Navitor Pharmaceuticals, Sarepta Therapeutics, Novartis, Verve Therapeutics, Silence Therapeutics, Veritas International, Color Health, Third Rock Ventures and Columbia University (NIH); received speaking fees from Illumina, MedGenome, Amgen, and the Novartis Institute for Biomedical Research; and received a sponsored research agreement from the Novartis Institute for Biomedical Research. M.C. holds equity in Waypoint Bio and is a member of the Nestle Scientific Advisory Board. A.R. is a co-founder and equity holder of Celsius Therapeutics, an equity holder in Immunitas Therapeutics and a scientific advisory board member of Thermo Fisher Scientific, Syros Pharmaceuticals, Asimov and Neogene Therapeutics. A.R. is also an employee of Genentech. All other authors declare no competing interests.

Additional information

Supplementary information The online version contains supplementary material available at https://doi.org/10.1038/s41586-022-04518-2.

Correspondence and requests for materials should be addressed to Evan D. Rosen.

Peer review information *Nature* thanks Bart Deplancke and the other, anonymous, reviewers for their contribution to the peer review of this work. Peer review reports are available.

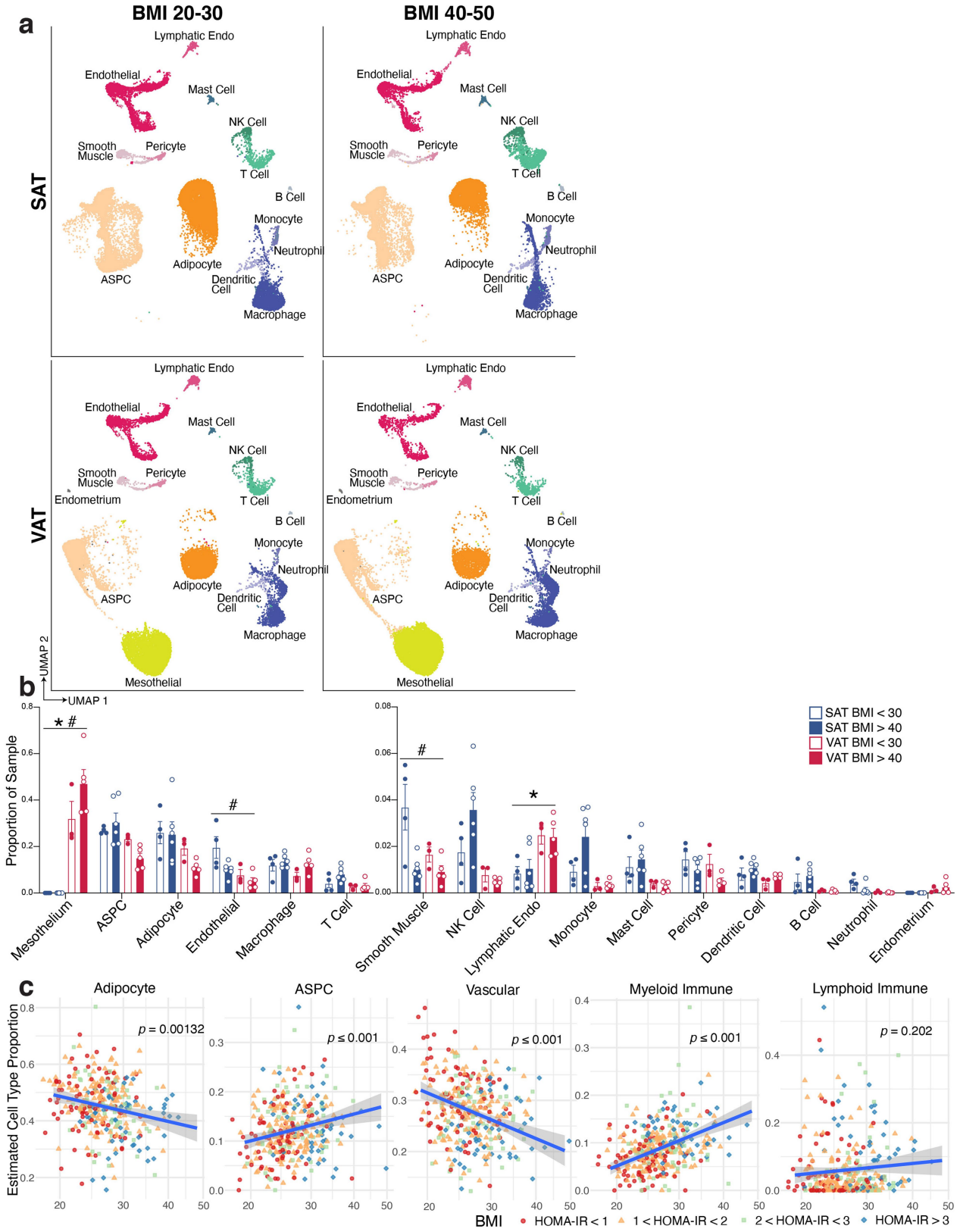

Extended Data Fig. 1 | See next page for caption.

Extended Data Fig. 1 | Additional analysis of the effects of depot and BMI on human WAT populations. a, UMAP projections of cells from the lowest and highest BMI ranges in the dataset, split by depot. To facilitate comparison, samples were randomly subset to contain the same number of cells in each plot (n = 20,339). **b**, Graph showing the proportion of sNuc-seq cells in each cluster per sample, split by depot and BMI, n = 4 SAT < 30, 6 SAT > 40, 3 VAT < 30, 5 VAT > 40. **C**, Estimated cell type proportions in bulk RNA sequencing data of subcutaneous adipose tissue from 331 individuals from the METSIM cohort calculated using sNuc-seq data as reference. Vascular cells include endothelial, lymphatic endothelial, pericytes, and smooth muscle cells. Myeloid immune includes macrophages, monocytes, dendritic cells, mast cells and neutrophils, and lymphoid immune includes B cells, NK cells, and T cells. For lines of best fit: Adipocytes $R^2 = 0.031$, ASPCs $R^2 = 0.034$, Vascular $R^2 = 0.076$, Myeloid Immune $R^2 = 0.13$, Lymphoid Immune $R^2 = 0.0049$. For scatterplots, error bands represent a confidence level of 0.95 and *P* values were calculated using an *F*-test with the null hypothesis that the slope = 0. For bar graphs, error bars represent SEM, * indicates credible depot effect and # indicates credible BMI effect, calculated using dendritic cells as reference.

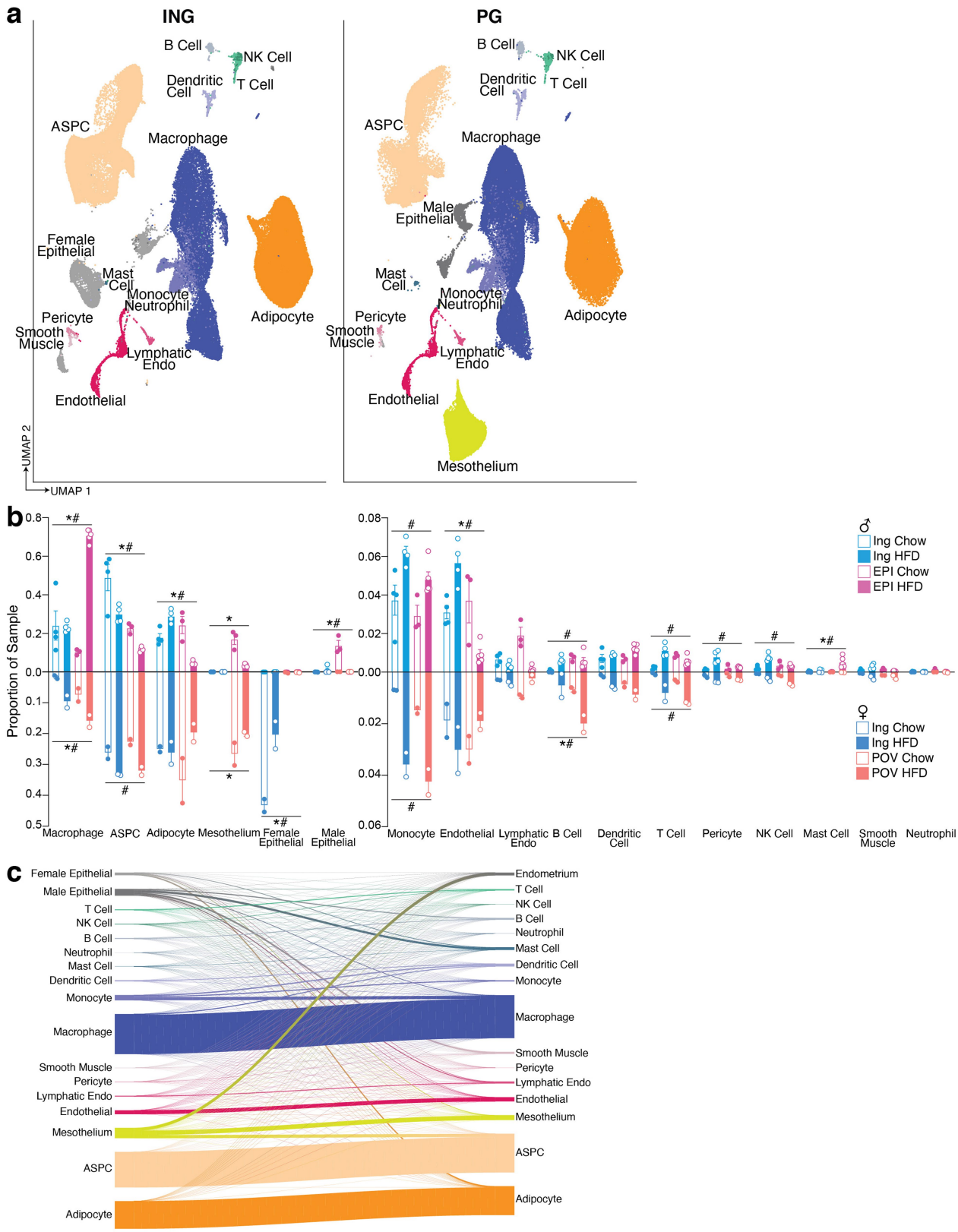

Extended Data Fig. 2 | Additional analysis of the effects of depot and diet on mouse WAT populations and association with human WAT populations. **a**, UMAP projection of all mouse WAT cells split by depot. **b**, Proportion of cells in each cluster per sample, split by sex as well as by depot and diet, for male mice n = 4 ING Chow, 4 ING HFD, 3 EPI Chow, and 5 EPI HFD. For female mice, n = 2 per condition. **c**, Riverplot showing the relationship between mouse and human clusters. Mouse cells were mapped onto human sNuc-seq cells using multimodal reference mapping. The riverplot represents the relationship between manually assigned mouse cluster and mapped human cluster for every mouse cell. For bar graphs, error bars represent SEM, * indicates credible depot effect and # indicates credible diet effect, calculated using dendritic cells as reference.

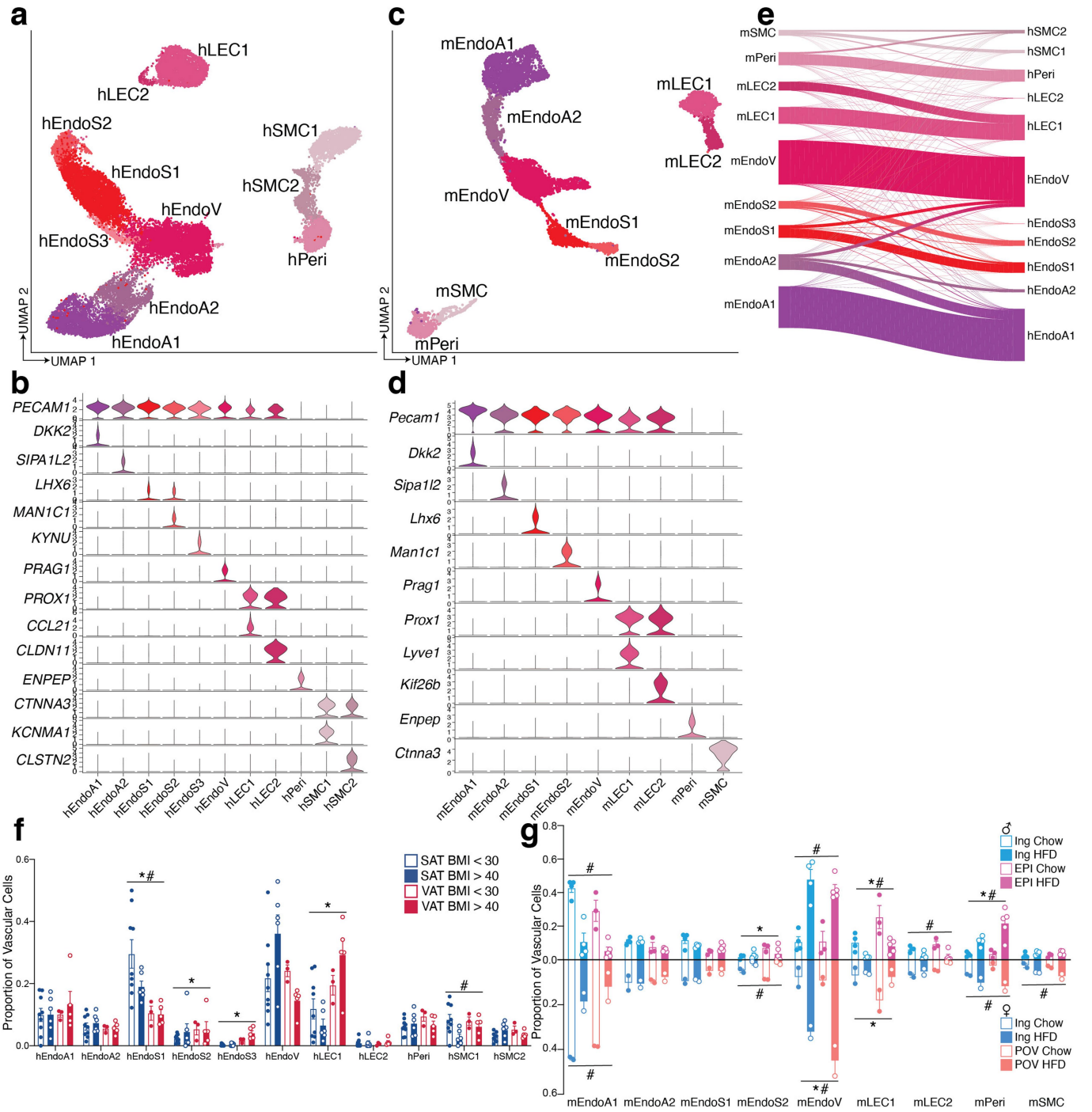

Extended Data Fig. 3 | Highly similar vascular cells in human and mouse WAT. a, UMAP projection of 22,734 human vascular cells. **b**, Marker genes for 11 distinct clusters of human WAT vascular cells. **c**, UMAP projection of 7,632 mouse vascular cells. **d**, Marker genes for 9 distinct clusters of mouse WAT vascular cells. **e**, Riverplot showing the correlation between annotated mouse and human vascular clusters based on multimodal reference mapping for each mouse cell. **f, g**, Bar graphs showing the proportion of cells in each cluster per sample split by depot and BMI for human (**f**) and depot, diet, and sex for mouse (**g**). For humans, n = 9 SAT < 30, 6 SAT > 40, 3 VAT < 30, and 5 VAT > 40. For male mice n = 4 ING Chow, 4 ING HFD, 3 EPI Chow, and 5 EPI HFD. For female mice, n = 2 per condition. For bar graphs, error bars represent SEM, * indicates credible depot effect and # indicates credible BMI/diet effect, calculated using hEndoA2 (human) and mEndoA2 (mouse) as reference.

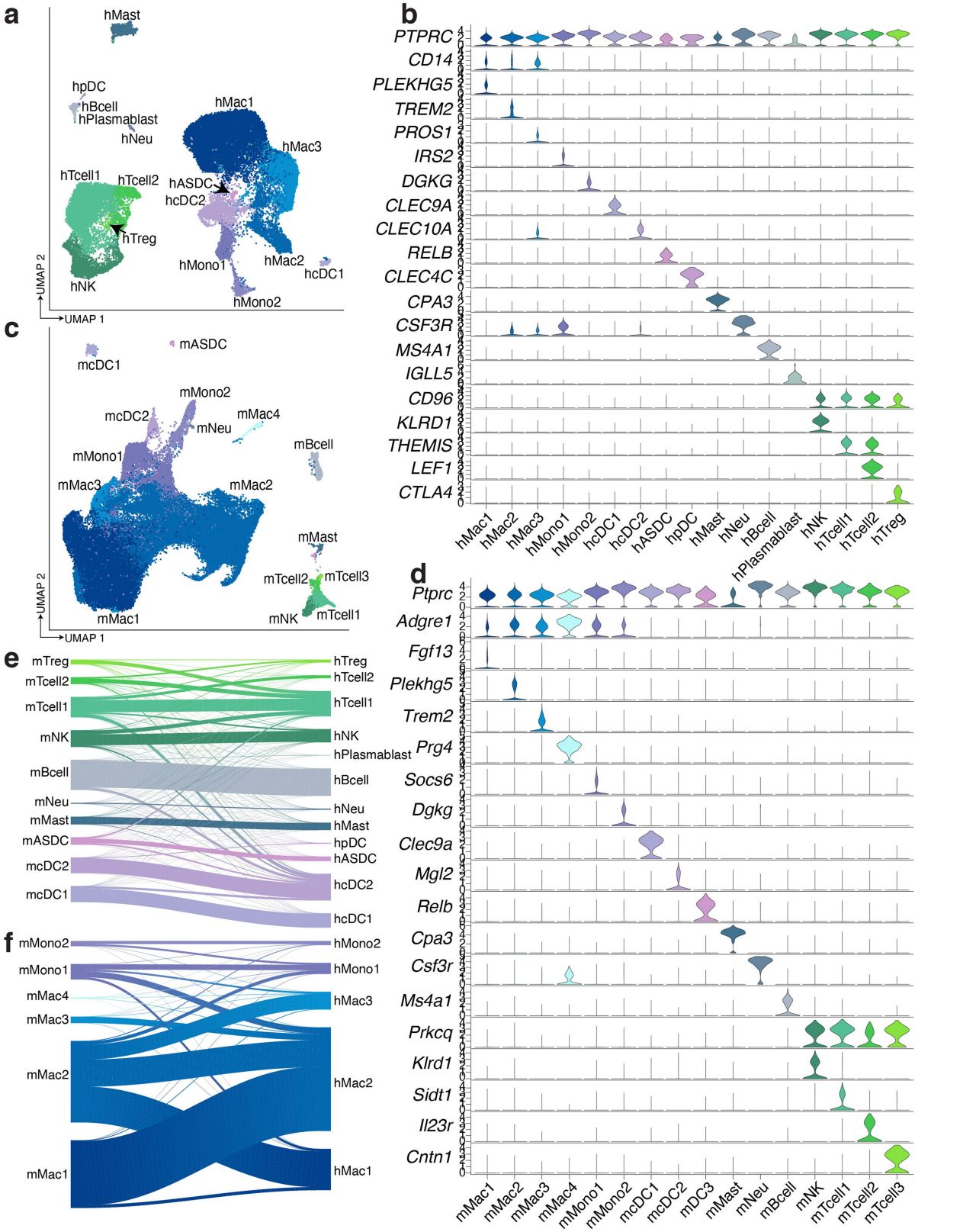

Extended Data Fig. 4 | Comparison of immune cells in human and mouse WAT. a, UMAP projection of 34,268 immune cells from human WAT. **b**, Marker genes for human immune cell clusters. **c**, UMAP projection of 70,547 immune cells from mouse WAT. **d**, Marker genes for mouse immune cell clusters. **e-f**, Riverplots showing the correlation between annotated mouse cluster and mapped human cluster for mouse (**e**) dendritic cells, mast cells, neutrophils, B cells, NK cells, and T cells and (**f**) monocytes and macrophages.

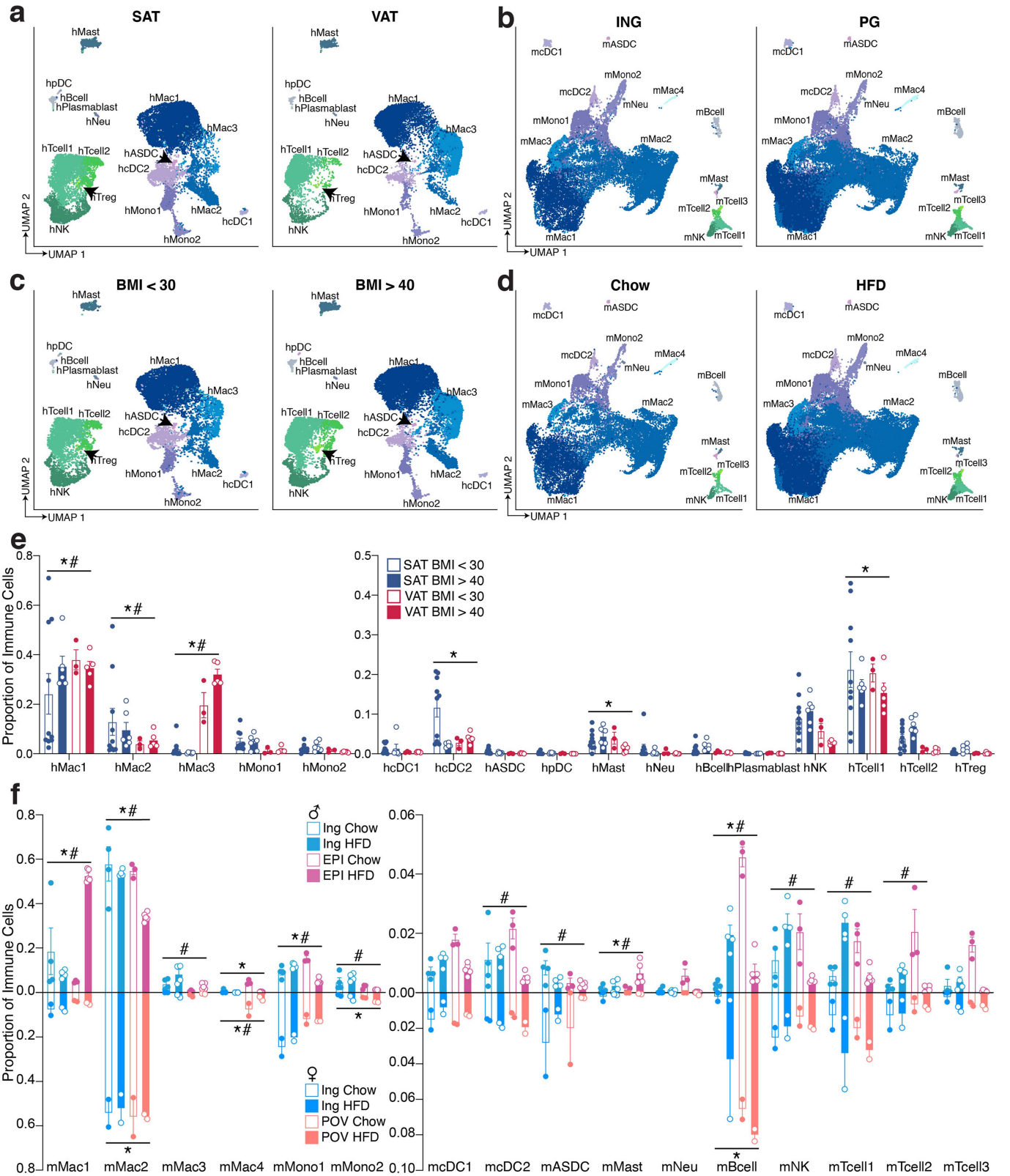

Extended Data Fig. 5 | Human and mouse immune cells are differentially regulated by depot and BMI/diet. a, **b**, UMAP projections of human (**a**) and mouse (**b**) WAT immune cells split by depot. **c, d**, UMAP projections of human (**c**) and mouse (**d**) WAT immune cells split by BMI (**c**) and diet (**d**). **e-f**, Bar graphs showing the proportion of cells in each cluster per sample split by depot and BMI for human (**e**) and depot, diet, and sex for mouse (**f**). For humans, n = 10 SAT < 30, 6 SAT > 40, 3 VAT < 30, and 5 VAT > 40. For male mice n = 4 ING Chow, 4 ING HFD, 3 EPI Chow, and 5 EPI HFD. For female mice, n = 2 per condition. For bar graphs, error bars represent SEM, * indicates credible depot effect and # indicates credible BMI/diet effect, calculated using hMono2 (human) and mcDC1 (mouse) as reference.

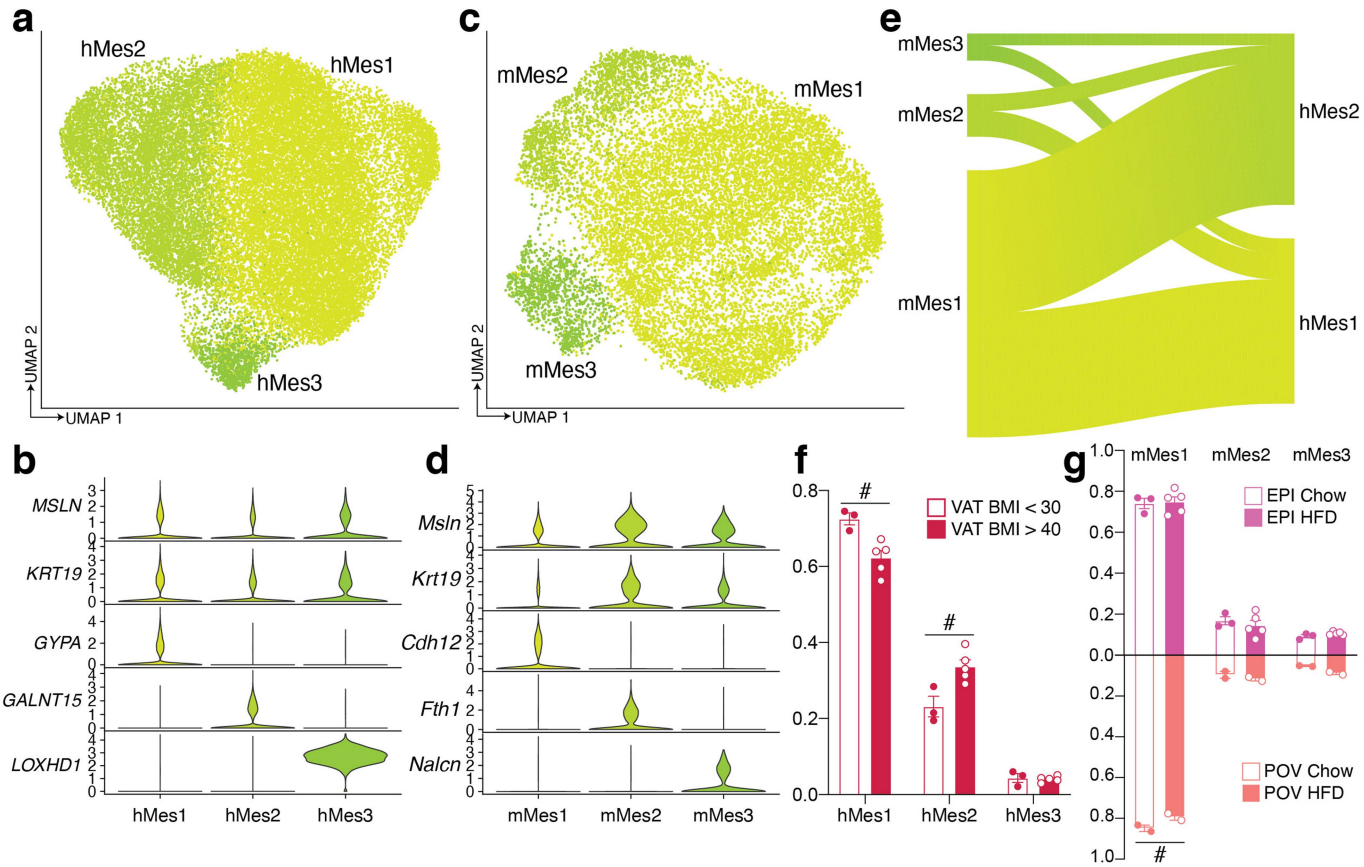

Extended Data Fig. 6 | Subpopulations of human and mouse mesothelial cells. a, UMAP projection of 30,482 human mesothelial cells. **b**, Marker genes for distinct human mesothelial populations. **c**, UMAP projection of 14,947 mouse mesothelial cells. **d** Marker genes for distinct mouse mesothelial populations. **e**, Riverplots showing relationship of mouse and human mesothelial clusters. **f, g**, Proportion of cells in each cluster per sample, split by BMI for human (**f**) and diet and sex for mouse (**g**). For humans, n = 3 VAT < 30, and 5 VAT > 40. For male mice n = 3 EPI Chow, and 5 EPI HFD. For female mice, n = 2 per condition. Error bars represent SEM, # indicates credible BMI/diet effect, calculated using hMes3 (human) and mMes1 (mouse) as reference.

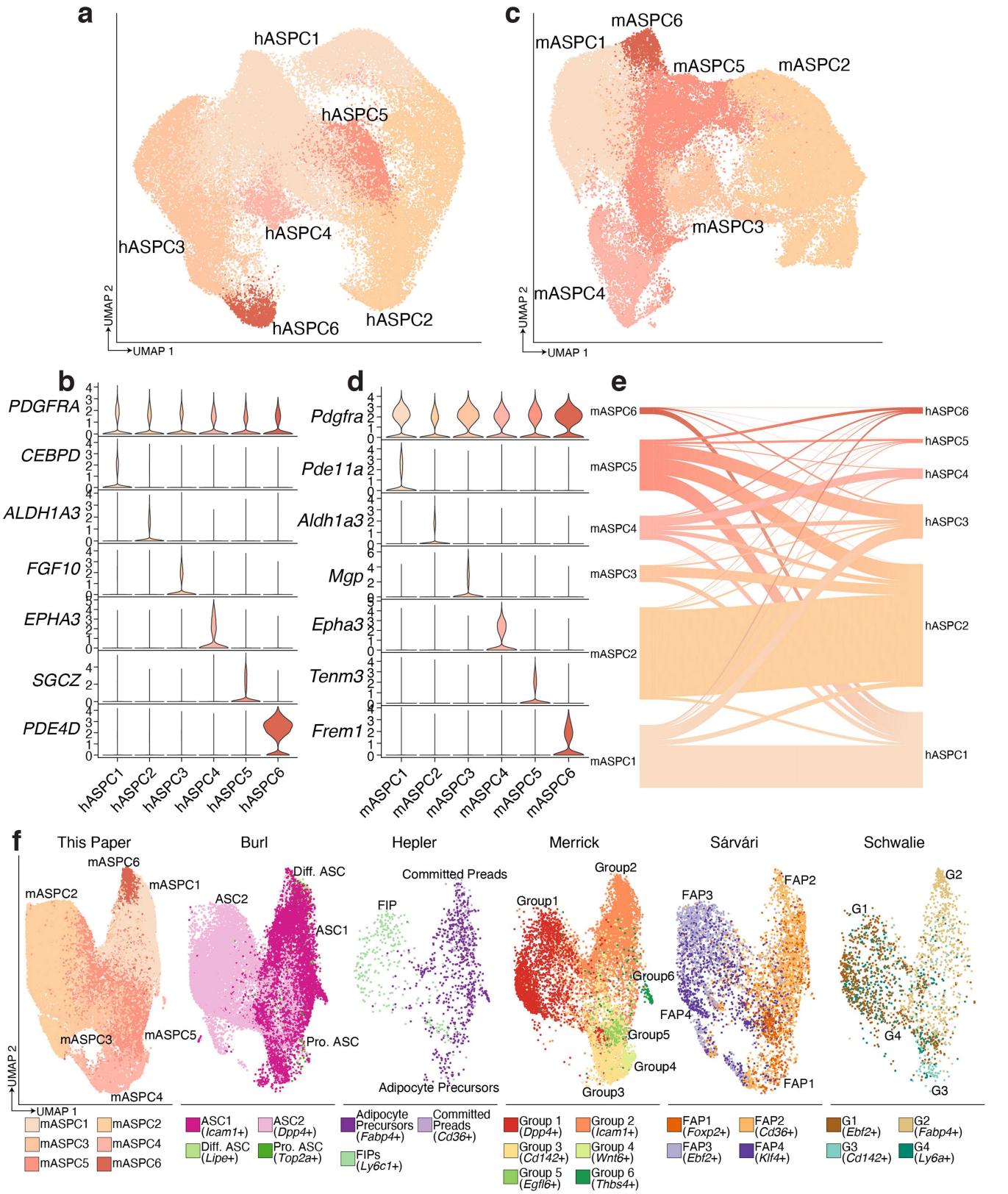

Extended Data Fig. 7 | Human and mouse ASPCs share commonalities with previously reported subtypes. a, UMAP projection of 52,482 human ASPCs. **b**, Marker genes for distinct ASPC subpopulations. **c**, UMAP projection of 51,227 mouse ASPCs. **d**, Marker genes for distinct ASPC subpopulations. **e**, Riverplot depicting the relationship between mouse and human ASPC clusters. **f**, Integration of ASPCs from this paper with ASPCs from other groups.

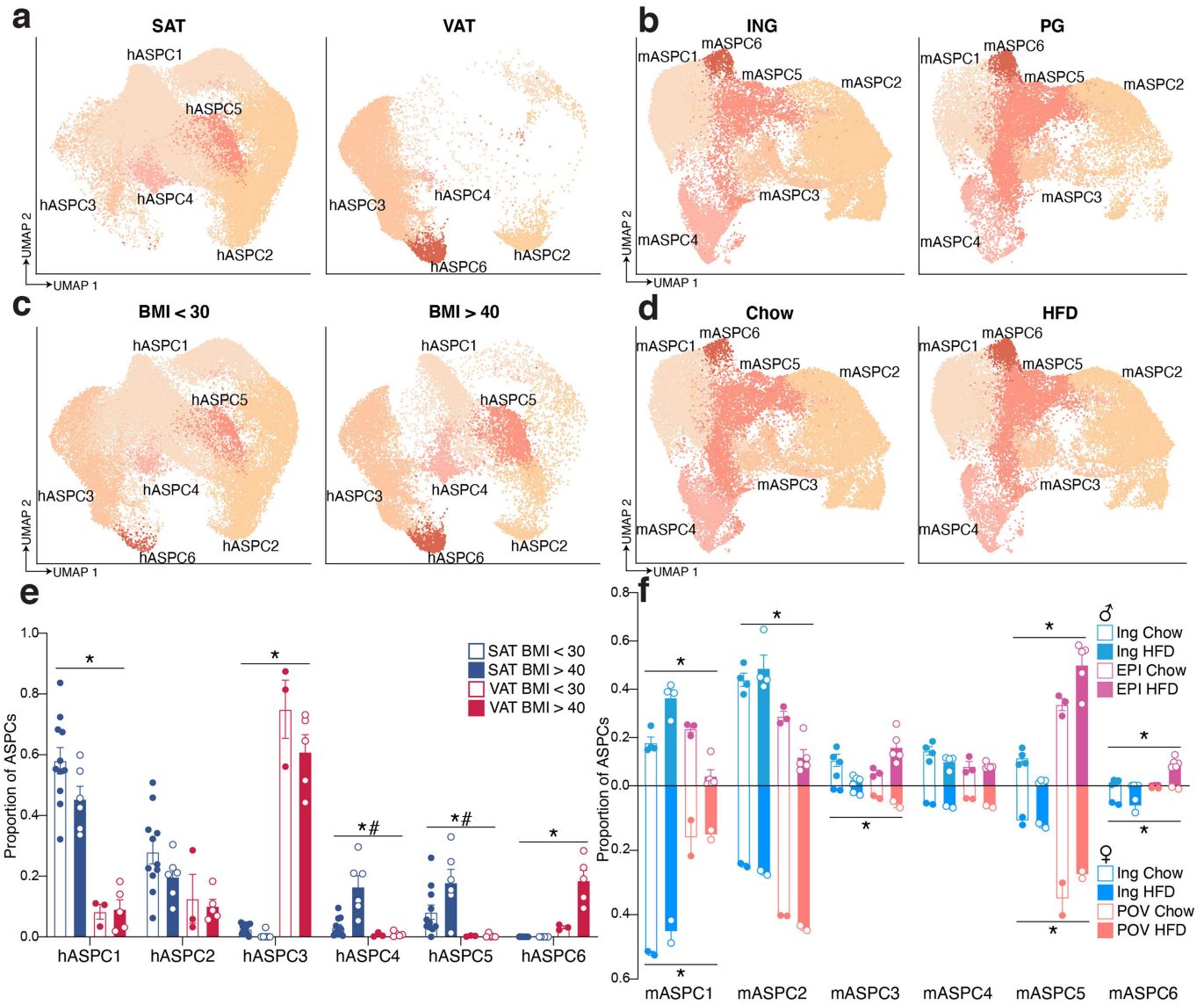

Extended Data Fig. 8 | Human ASPCs exhibit strong depot dependency while mouse ASPCs are dependent on both depot and diet. a, **b**, UMAP projections of human (**a**) and mouse (**b**) ASPCs split by depot. **c**-**d**, UMAP projections of human (**c**) and mouse (**d**) ASPCs split by BMI/diet. **e**, **f**, Proportion of ASPC cells in each cluster per sample split by depot and BMI for human (**e**) and depot, diet, and sex for mouse (**f**). For humans, n = 11 SAT < 30, 6 SAT > 40, 3 VAT < 30, and 5 VAT > 40. For male mice n = 4 ING Chow, 4 ING HFD, 3 EPI Chow, and 5 EPI HFD. For female mice, n = 2 per condition. For bar graphs, error bars represent SEM, * indicates credible depot effect and # indicates credible BMI/diet effect, calculated using hASPC2 (human) and mASPC4 (mouse) as reference.

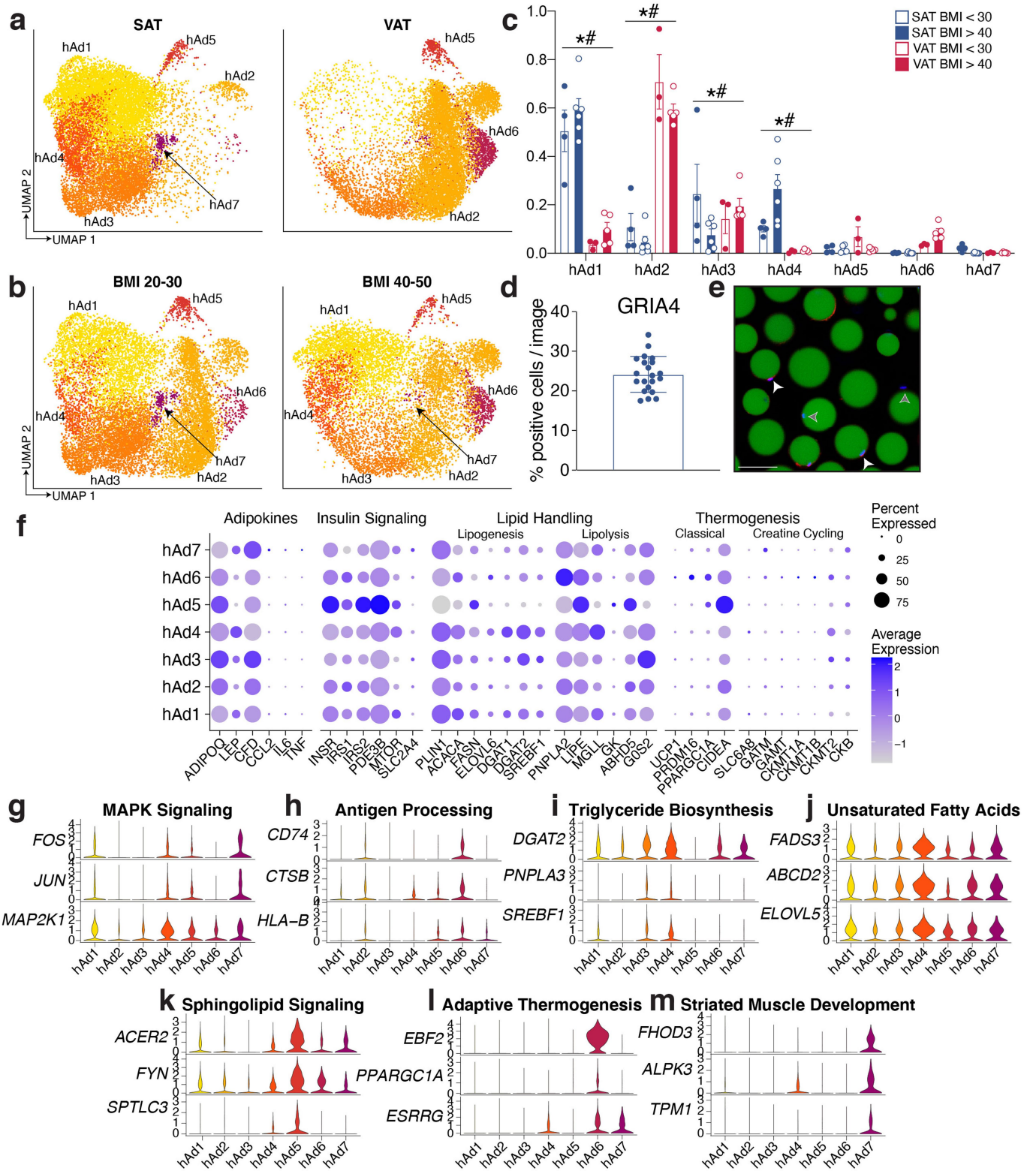

Extended Data Fig. 9 | Human adipocyte subtypes are highly dependent on depot and may be responsible for distinct functions. a, **b**, UMAP projections of human white adipocytes split by depot (**a**) and BMI (**b**). **c**, Proportion of cells in each human cluster by sample split by depot and BMI, n = 4 SAT < 30, 6 SAT > 40, 3 VAT < 30, and 5 VAT > 40. **D**, Quantification of immunofluorescence analysis of GRIA4+ cells in mature human adipocytes from two individuals. Each dot represents an image, n = 12 images from individual 1 and 9 images from individual 2 with a total of 704 counted cells. Only cells with visible nuclei were included in the quantification. **e**, Representative image of GRIA4+ cells, white arrows represent positive cells, grey represent negative, scale bar = 100 µm. In total, there were 21 images from samples taken from two individuals. **f**, Expression of genes associated with adipokine secretion, insulin signaling, lipid handling, and thermogenesis across human adipocyte subclusters. **g**–**m**, Expression of genes associated with GO or KEGG pathways indicative of individual human adipocyte subclusters. For bar graph, error bars represent SEM, * indicates credible depot effect and # indicates credible BMI effect, calculated using hAd5 as reference.

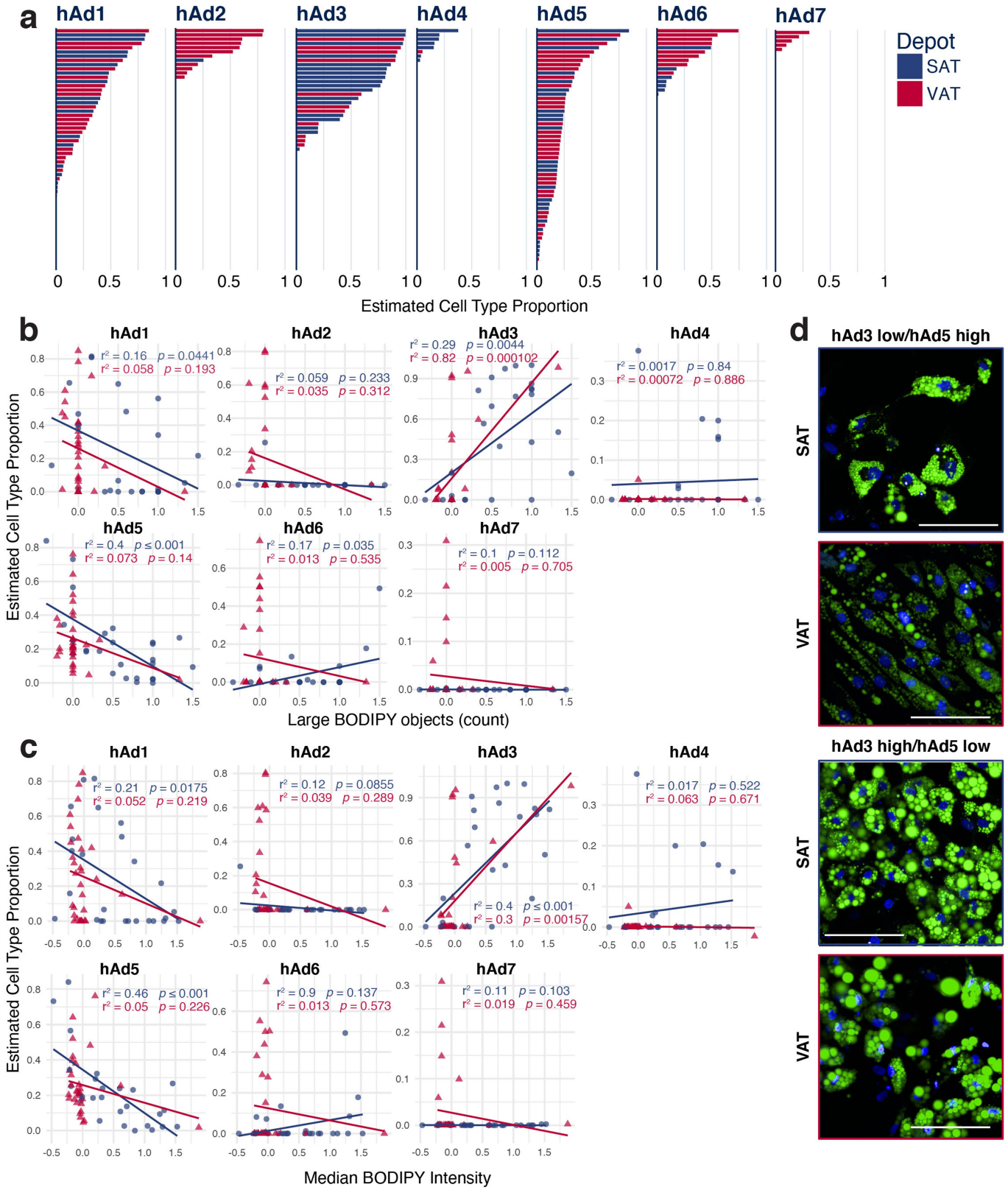

Extended Data Fig. 10 | Human adipocytes differentiated *ex vivo* recapitulate many of the adipocyte subclusters found in vivo. a, Plot of estimated cell type proportion in *ex vivo* adipocyte cultures differentiated from subcutaneous or visceral preadipocytes for 14 days, ordered by estimated proportion. **b, c**, Scatterplots showing the relationship between estimated cell type proportion and the LipocyteProfiler-calculated features Large BODIPY objects (**b**) and Median BODIPY Intensity (**c**). *p* values were calculated using an *F*-test with the null hypothesis that the slope = 0. **d**, Representative images of hAd3 low/hAd5 or hAd3 high hAd5 low *ex vivo* differentiated cultures. Green represents BODIPY staining, blue represents Hoechst staining. Scale bars are 100 µm, in total, 3 randomly selected images/sample were analyzed from 3 SAT samples and 3 VAT samples with the lowest and highest predicted proportions of hAd3 and hAd5.

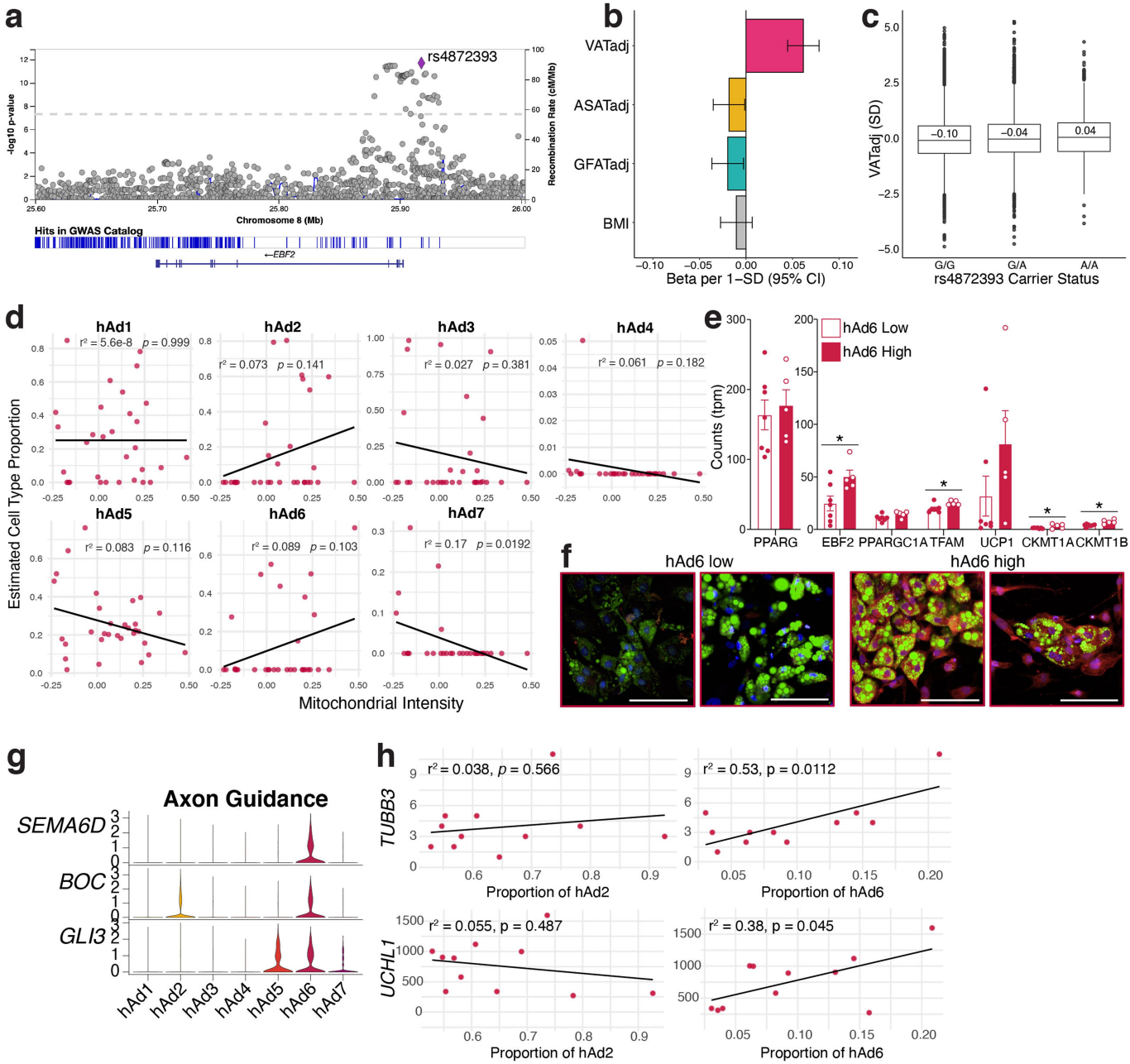

Extended Data Fig. 11 | Visceral-specific adipocyte subpopulation hAd6 is associated with thermogenic traits. a, Regional visualization of associations of common genetic variants near EBF2 with VATadj. **b**, Effect size of association of rs4872393 with VATadj, ASATadj, GFATadj, and BMI per minor allele A; n = 37,641. Error bars reflect a 95% confidence interval around the effect size estimate from regression. **c**, VATadj raw data plotted according to rs4872393 carrier status; n = 36,185. For box plots, horizontal line = median, lower and upper bounds of the box = 1st and 3rd quartile respectively, lower and upper whisker = 1st quartile − 1.5 x interquartile range (IQR) and 3rd quartile + 1.5 x IQR respectively, outliers are plotted as points. **d**, Scatterplot showing the relationship between estimated cell type proportion and the LipocyteProfiler calculated feature Mitochondrial Intensity in visceral samples. **e**, Expression of mitochondrial and thermogenic genes in visceral *ex vivo* differentiated adipocytes stratified by estimated hAd6 proportion and matched for amount of differentiation using *PPARG* expression, n = 7 mAd6 low and 5 mAd6 high. Error bars represent SEM, *P* values were calculated using two tailed t-tests with no adjustments for multiple comparison, *, $P < .05$, **, $P < .01$. Exact *P* values: *EBF2* = 0.027, *TFAM* = 0.019, *CKMT1A* = 0.049, *CKMT1B* = 0.005. **f**, Representative images of hAd6 low and high visceral in vitro differentiated cultures. Green represents BODIPY staining, red represents MitoTracker staining, and blue represents Hoechst staining. Scale bars are 100 µm, in total 3 random images/sample were analyzed from 5 hAd6 low and 5 hAd6 high samples. **g**, Violin plot of sNuc-seq data showing axon guidance genes in adipocyte subclusters. **h**, Scatterplots showing the relationship between calculated proportion of visceral subpopulations hAd2 and hAd6 and expression of pan-neuronal markers on the ambient RNA of individual visceral sNuc-seq samples. For scatterplots, *P* values were calculated using an *F*-test with the null hypothesis that the slope = 0.

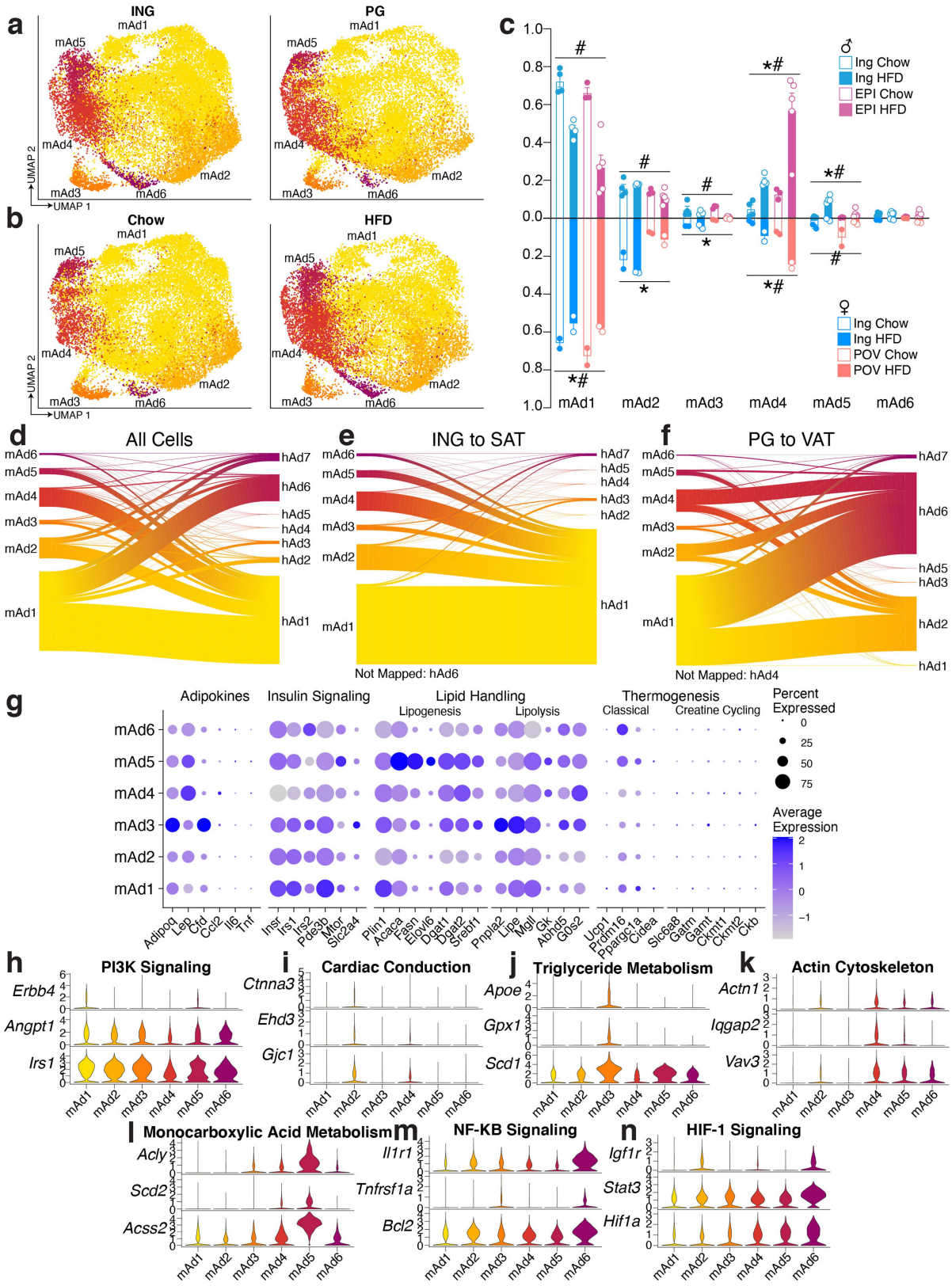

Extended Data Fig. 12 | Mouse adipocytes appear to have distinct functionality but are not analogous to human adipocyte subpopulations. **a**, **b**, UMAP projections of mouse adipocytes split by depot (**a**) and diet (**b**). **c**, Proportion of cells in each mouse cluster per sample split by depot, diet, and sex. For male mice n = 4 ING Chow, 4 ING HFD, 3 EPI Chow, and 5 EPI HFD. For female mice, n = 2 per condition. **d**, Expression of genes associated with known adipocyte functions in mouse adipocyte subclusters. **e**–**k**, Expression of genes associated with GO or KEGG pathways indicative of individual mouse adipocyte subclusters. **l**–**n**, Riverplots of mouse cells showing the association between mouse and human adipocyte clusters from both subcutaneous and visceral depots (**l**), subcutaneous (ING and SAT) adipocytes only (**m**) or visceral (PG and VAT) adipocytes only (**n**). For depot comparisons, both mouse query objects and human reference objects were subset to the respective depot before mapping. For bar graph, error bars represent SEM, * indicates credible depot effect and # indicates credible diet effect, calculated using mAd6 as reference.

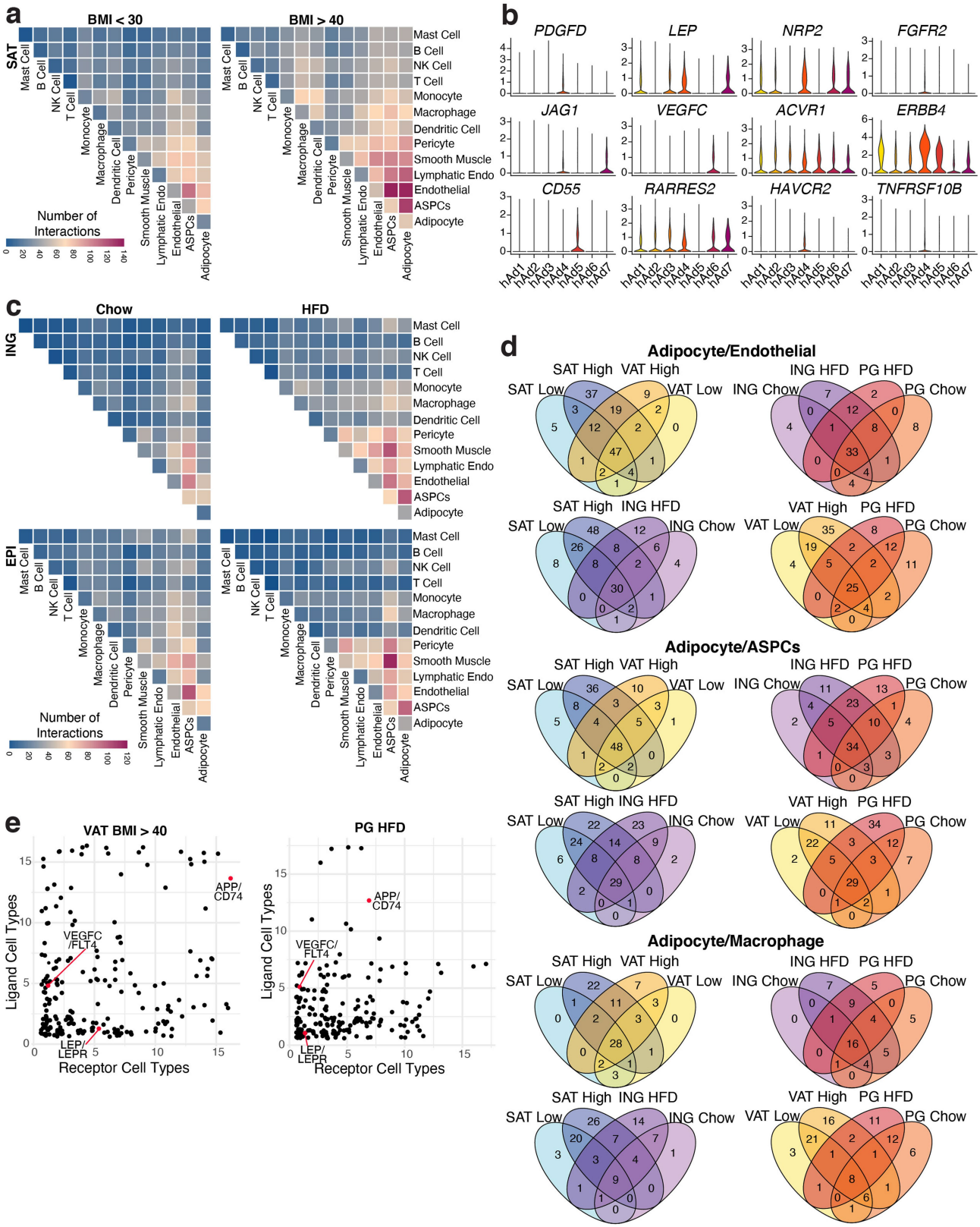

Extended Data Fig. 13 | CellphoneDB identifies increasing numbers of cell-cell interactions within WAT during obesity. a, Heatmap showing number of significant interactions identified between cell types in SAT of low (<30) and high (>40) BMI individuals as determined by CellphoneDB. **b**, Expression of ligand and receptor genes from Fig. 4b in human adipocyte subclusters. **c**, Heatmaps showing number of significant interactions identified between cell types in ING and PG WAT of chow and HFD fed mice. **d**, Venn diagrams showing the overlap of significant interactions between adipocytes and endothelial cells, ASPCs, and macrophages between depot, BMI/diet, and species. **e**, Jitter plots of the relationship between number of WAT cell types expressing a ligand (y axis) vs. the number of cell types expressing the receptor (x axis) for all significant interactions in high BMI human VAT (left) and mouse HFD PG (right).

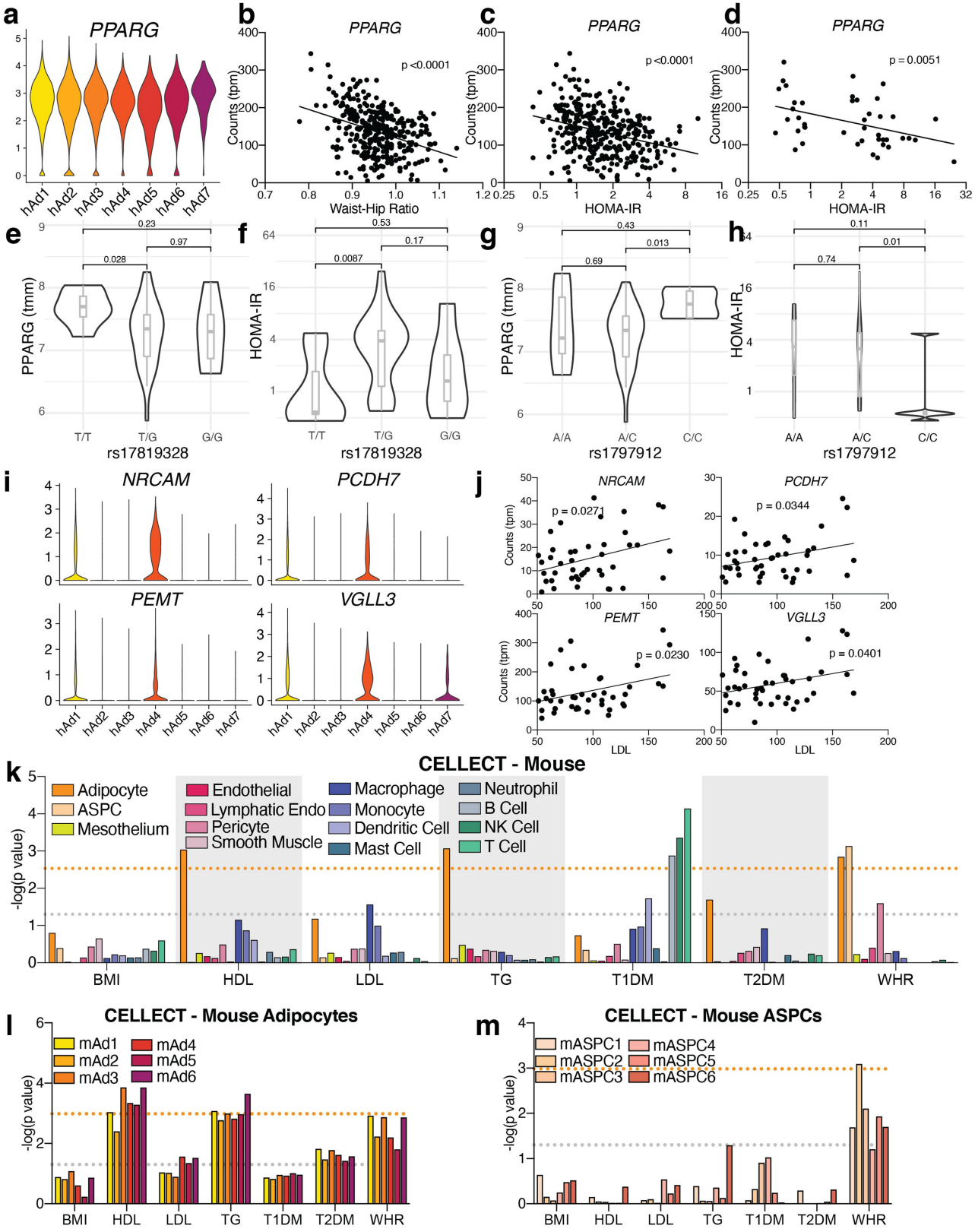

Extended Data Fig. 14 | See next page for caption.

Extended Data Fig. 14 | Association with GWAS data provides further insight into the contribution of white adipocytes to human traits. a-c, Expression of *PPARG* in human adipocyte subclusters (**a**), and in METSIM SAT bulk RNA-seq plotted against WHR (**b**) or HOMA-IR (**c**). **d**, Expression of *PPARG* in isolated subcutaneous adipocyte bulk RNA-seq plotted against HOMA-IR. **e-h**, SNPs in the *PPARG* gene identified by DEPICT as associated with BMI-adjusted WHR plotted against *PPARG* gene expression (**e, g**) and HOMA-IR (**f, h**) in isolated subcutaneous adipocyte bulk RNA-seq data and cohort. For rs17819328 n = 7 for T/T, 30 for T/G, and 6 for G/G. For rs1797912 n = 7 for A/A, 31 for A/C, and 5 for C/C. For box plots, horizontal line = median, lower and upper bounds of the box = 1st and 3rd quartile respectively, lower and upper whisker = 1st quartile − 1.5 x interquartile range (IQR) and 3rd quartile + 1.5 x IQR respectively. *P* values were calculated using a Wilcoxin test. **i-j**, Expression of genes in human adipocyte subtypes from sNuc-seq data (**i**) and from isolated subcutaneous adipocyte bulk RNA-seq plotted against LDL (**j**). **k**, *p* values of the association between mouse cell types and GWAS studies. **l**–**m**, *p* values of the association between mouse adipocyte (**l**) or ASPC (**m**) subclusters with GWAS studies. For all graphs, the grey line represents $P = 0.05$ and the orange line represents significant *P* value after Bonferroni adjustment ($P = 0.003$ for all cell, $P = 0.001$ for subclusters), calculated based on number of cell types queried. For scatterplots, *P* values were calculated using an *F*-test with the null hypothesis that the slope = 0.

Extended Data Table 1 | Subject information for Drop-Seq, sNuc-seq, and bulk RNA-seq of isolated subcutaneous human adipocytes

Subjects for Drop-Seq

Subject	BMI	Age	Sex	Race/Ethnicity	SAT	Surgery	Institution
Hs235	36.04	53	F	Caucasian	Pannus	Panniculectomy	BIDMC
Hs236	25.74	35	F	Caucasian	Thigh	Thighplasty	BIDMC
Hs237	22.59	53	F	Caucasian	Pannus	DIEP	BIDMC
Hs238	19.57	49	F	Caucasian	Pannus	Abdominoplasty	BIDMC
Hs239	24.8	71	F	Caucasian	Pannus	DIEP	BIDMC
Hs240	25.82	59	F	Caucasian	Pannus	Panniculectomy	BIDMC
Hs242	22.88	59	F	Caucasian	Pannus	DIEP	BIDMC
Hs248	32.28	68	F	Caucasian	Pannus	Panniculectomy	BIDMC
Hs249	26.46	54	F	Caucasian	Pannus	DIEP	BIDMC

DIEP: Deep inferior epigastric perforators

Subjects for sNuc-seq

Subject	BMI	Age	Sex	Race/ Ethnicity	SAT	VAT	Surgery	Institution
Hs001	49.3	29	F	Caucasian	Periumbilical	Omental	VSG	UPitt
Hs002	33.1	57	F	Caucasian	Periumbilical	NA	Hernia	UPitt
Hs004	25.4	51	F	Caucasian	Periumbilical	NA	CCY	UPitt
Hs009	45.7	41	F	Black	Periumbilical	Omental	VSG	UPitt
Hs010	43.1	35	F	Caucasian	Periumbilical	Omental	RYGB	UPitt
Hs011	42.8	58	F	Black	Periumbilical	NA	VSG	UPitt
Hs012	48.7	36	M	Caucasian	Periumbilical	Omental	VSG	UPitt
Hs013	43.2	24	M	Caucasian	Periumbilical	Omental	VSG	UPitt
Hs253	30.04	53	F	Caucasian	Periumbilical	Preperitoneal	TAH BSO	BIDMC
Hs254	23.96	41	F	Caucasian/ Hispanic	Periumbilical	Preperitoneal	TAH BSO	BIDMC
Hs255	24.27	73	F	Caucasian	Periumbilical	Preperitoneal	TAH BSO	BIDMC
Hs256	34.53	41	F	Black	Periumbilical	Omental	CCY	BIDMC
Hs266	22.15	68	M	Caucasian	Periumbilical	Omental	Colon polyp	BIDMC

Bulk RNA-seq of floated adipocytes

	Insulin Sensitive average(min-max)	**Insulin Resistant** average(min-max)	***p* Value**
N	16	27	
AGE	47.3 (36-63)	50.6 (33-71)	0.289
BMI	27.2 (21-33)	30.1 (21-42)	0.042
HOMA-IR	0.70 (0.46-0.88)	5.8 (2.1-24.5)	0.00012
HDL	70.5 (42-154)	54.1 (26-100)	0.022
LDL	93.2 (54-133)	97.9 (51-169)	0.651

BMI, age, sex, race/ethnicity, depot, fat location, and surgery information for all Drop-Seq and sNuc-seq subjects as well as information for insulin sensitive and insulin resistant bulk RNA-seq adipocyte cohort. *P* values were calculated using two tailed t-tests with no adjustment for multiple comparisons.

Abbreviations: VSG: Vertical sleeve gastrectomy; CCY: Cholecystectomy; RYGB: Roux en Y gastric bypass; TAH BSO: Total abdominal hysterectomy and bilateral salpingo-oophorectomy.

Extended Data Table 2 | Numbers of cells in human and mouse single cell experiments broken down by cluster, depot, BMI/ diet, and technology

Human Cell Numbers

	VAT			SAT							
	sNuc			sNuc			Drop		VAT total	SAT total	Total
BMI	< 30	30-40	> 40	< 30	30-40	> 40	< 30	> 30			
Adipocyte	5211	1011	5253	7611	2847	3938	0	0	11475	14396	25871
ASPCs	5938	1404	7304	6848	2703	7329	15195	5761	14646	37836	52482
Mesothelium	7773	1927	20782	0	0	0	0	0	30482	0	30482
Endothelial	2351	1030	2345	4231	2783	2059	577	107	5726	9757	15483
Lymphatic Endo	677	240	1138	195	130	305	168	48	2055	846	2901
Pericyte	381	109	254	353	132	172	60	3	744	720	1464
Smooth Muscle	448	360	423	709	621	237	83	5	1231	1655	2886
Macrophage	1908	630	6328	3121	1795	2871	1256	403	8866	9446	18312
Monocyte	98	41	173	187	155	549	359	387	312	1637	1949
Dendritic Cell	125	30	340	169	119	188	756	714	495	1946	2441
Mast Cell	111	27	139	210	294	298	66	23	277	891	1168
Neutrophil	7	9	4	98	12	14	0	2	20	126	146
B Cell	28	12	39	57	49	188	30	26	79	350	429
NK Cell	229	92	242	375	279	669	297	446	563	2066	2629
T Cell	762	382	1661	667	510	1522	977	713	2805	4389	7194
Endometrium	45	150	114	0	0	0	2	1	309	3	312
Total	26092	7454	46539	24831	12429	20339	19826	8639	80085	86064	166149

Mouse Cell Numbers

	PG		Ing				
	Chow	HFD	Chow	HFD	PG Total	Ing Total	Total
Adipocyte	12874	5139	8645	13276	18013	21921	39934
ASPCs	9928	10194	16308	14797	20122	31105	51227
Mesothelium	10074	4873	0	0	14947	0	14947
Endothelial	1521	673	1141	2261	2194	3402	5596
Lymphatic Endo	678	101	224	173	779	397	1176
Pericyte	62	170	56	309	232	365	597
Smooth Muscle	56	52	30	125	108	155	263
Macrophage	3788	35673	9370	9017	39461	18387	57848
Monocyte	975	2801	1286	2545	3776	3831	7607
Dendritic Cell	268	688	237	379	956	616	1572
Mast Cell	4	267	13	27	271	40	311
Neutrophil	23	9	8	7	32	15	47
B Cell	301	594	28	279	895	307	1202
NK Cell	110	215	67	282	325	349	674
T Cell	266	472	69	479	738	548	1286
Male Epithelial	3463	36	19	329	3499	348	3847
Female Epithelial	76	45	6331	3135	121	9466	9587
Total	44467	62002	43832	47420	106469	91252	197721

Cell counts per cluster for human and mouse data broken down by technology, depot, and BMI/diet.

Extended Data Table 3 | GWAS studies used for CELLECT analysis

Trait	Study/collection
BMI	Pulit, S. L. et al. Meta-analysis of genome-wide association studies for body fat distribution in 694 649 individuals of European ancestry.
HDL	https://alkesgroup.broadinstitute.org/sumstats_formatted/
LDL	https://alkesgroup.broadinstitute.org/sumstats_formatted/
T1D	https://alkesgroup.broadinstitute.org/sumstats_formatted/
T2D (BMI adjusted)	Mahajan, A. et al. Fine-mapping type 2 diabetes loci to single-variant resolution using high-density imputation and islet-specific epigenome maps.
Triglycerides	https://alkesgroup.broadinstitute.org/sumstats_formatted/
WHR (BMI adjusted)	Loh, P.-R., Kichaev, G., Gazal, S., Schoech, A. P. & Price, A. L. Mixed-model association for biobank-scale datasets

List of sources for GWAS datasets used in the CELLECT analysis.

nature research

Corresponding author(s): Evan D Rosen

Last updated by author(s): 2022/1/13

Reporting Summary

Nature Research wishes to improve the reproducibility of the work that we publish. This form provides structure for consistency and transparency in reporting. For further information on Nature Research policies, see our Editorial Policies and the Editorial Policy Checklist.

Statistics

For all statistical analyses, confirm that the following items are present in the figure legend, table legend, main text, or Methods section.

n/a	Confirmed	
☐	☒	The exact sample size (*n*) for each experimental group/condition, given as a discrete number and unit of measurement
☐	☒	A statement on whether measurements were taken from distinct samples or whether the same sample was measured repeatedly
☐	☒	The statistical test(s) used AND whether they are one- or two-sided *Only common tests should be described solely by name; describe more complex techniques in the Methods section.*
☐	☒	A description of all covariates tested
☐	☒	A description of any assumptions or corrections, such as tests of normality and adjustment for multiple comparisons
☐	☒	A full description of the statistical parameters including central tendency (e.g. means) or other basic estimates (e.g. regression coefficient) AND variation (e.g. standard deviation) or associated estimates of uncertainty (e.g. confidence intervals)
☐	☒	For null hypothesis testing, the test statistic (e.g. *F*, *t*, *r*) with confidence intervals, effect sizes, degrees of freedom and *P* value noted *Give P values as exact values whenever suitable.*
☐	☒	For Bayesian analysis, information on the choice of priors and Markov chain Monte Carlo settings
☒	☐	For hierarchical and complex designs, identification of the appropriate level for tests and full reporting of outcomes
☒	☐	Estimates of effect sizes (e.g. Cohen's *d*, Pearson's *r*), indicating how they were calculated

Our web collection on statistics for biologists contains articles on many of the points above.

Software and code

Policy information about availability of computer code

Data collection	No software was used to collect the data in this study.
Data analysis	Single-cell/nucleus RNA-seq data analysis. Raw sequencing reads were demultiplexed to FASTQ format files using bcl2fastq (Illumina; version 2.20.0). Digital expression matrices were generated from the FASTQ files using the Drop-Seq tools (https://github.com/broadinstitute/Drop-seq, version 2.4.0) pipeline, with appropriate adjustments made to the default program parameters to account for the different read-structures in the scRNA Drop-Seq data and sNuc 10X data. Reads from mouse and human were aligned with STAR (version 2.7.3) against the GRCm38 and GRCh38 genome assemblies, respectively. Gene counts were obtained, per-droplet, by summarizing the unique read alignments across exons and introns in appropriate GENCODE annotations (release 16 of the mouse annotation and release 27 of the human annotation). In order to adjust for downstream effects of ambient RNA expression within mouse nuclei (hereafter "cells"), we used CellBender (version 0.2.0) to remove counts due to ambient RNA molecules from the count matrices and to estimate the true cells. We also used CellBender to distinguish droplets containing cells from droplets containing only ambient RNA, by selecting droplets with >50% posterior probability of containing a cell. We compared the true cell estimation obtained using CellBender against the same using the DropletUtils software package, which estimates ambient RNA expression levels but does not remove any ambient counts, keeping only the cells that were marked as not ambient by both algorithms. To address ambient RNA in the human sNuc data, we calculated spliced and unspliced RNA content in each cell, because nuclei have a high unspliced RNA content, a high percentage of spliced RNA indicates a high ambient RNA content. We therefore removed sNuc-seq cells containing over 75% spliced RNA. All samples were assessed for doublet content using scrublet version 0.2.1, and cells called as doublets were removed before further analysis. All cells were further filtered to have greater than 400 UMIs with <10% of UMIs from mitochondrial genes. Genes were filtered such that only genes detected in two or more cells were retained. For the human data, the median number of UMIs detected per cell was 2559 and the median number of genes detected per cell was 1524. For the mouse data, the median number of UMIs detected per cell was 2291 and the median number of genes detected per cell was 1369. The code used to perform this data analysis can be found at https://gitlab.com/rosen-lab/white-adipose-atlas.

Bulk RNA-seq Analysis.
Sequencing reads were demultiplexed by using bcl2fastq (Illumina). Salmon (version 1.1.0)as used to simultaneously map and quantify transcript abundances of hg19 genes annotated by release 19 of the GENCODE project's human reference. Salmon was run using "full" selective alignment (SAF) with mapping validation as described previously58. Gene counts were summarized from transcript abundances using the "tximport" package for R. The code used to perform this analysis can be found at https://gitlab.com/rosen-lab/white-adipose-atlas.

Integration, clustering and subclustering analysis were performed using Seurat 3.9.9. Data was normalized using SCTransform, and regressed on mitochondrial read percentage, ribosomal read percentage, and cell cycle score as determined by Seurat. In order to avoid smoothing over depot differences, for integration human and mouse data were grouped by 'individual', i.e., if both subcutaneous and visceral adipose tissue for an individual human or mouse were available they were pooled together during this step. Individuals were integrated with reciprocal PCA, using individuals that had both subcutaneous and visceral samples as references. As a result, the human and mouse references were comprised exclusively from the sNuc seq cohort. All sNuc seq individuals with only subcutaneous data as well as all Drop-seq samples were mapped to the reference. For clustering, ribosomal and mitochondrial genes were removed from the variable gene set before running PCA and calculating clusters. Clusters were identified as adipocytes, preadipocytes, mesothelial cells, vascular cells, or immune cells using marker genes, subset into individual objects, and re-integrated using the above method. Samples with fewer than 50 cells in the subset were removed before re-integration. This led to samples having artificially fewer cells in some instances—for example some Drop-seq samples had cells that clustered with adipocytes, but these cells were removed in subclustering because the small numbers of cells introduced too much variability into the integration. In the subclustered objects, we removed clusters that appeared to represent doublets based on the score assigned by scrublet, or that appeared to be driven by high ambient RNA content as determined by levels of mitochondrial genes and spliced/unspliced RNA ratio. The remaining clusters were annotated based on marker gene expression. In some cases, smaller subclusters such as T and NK cells were further subset and PCA and clustering analysis but not integration was re-run in order to assign clusters. After subcluster annotation, identities were mapped back onto the original object and cells that were removed from the subclustered objects were similarly removed from the all-cell object. The code used to perform clustering and subclustering analysis can be found at https://gitlab.com/rosen-lab/white-adipose-atlas.

Deconvolution of bulk RNA-seq data
Bulk RNA sequencing data for subcutaneous adipose tissue from the METSIM cohort were obtained as described previously. Only individuals with available metabolic phenotyping data were used for the deconvolution analysis. Bulk RNA sequencing data for floated human adipocytes were obtained described above. Deconvolution analysis was performed using MuSiC (version 0.1.1) with human sNuc subcutaneous all cell or adipocyte data as reference.

Comparison between mouse and human datasets
Mapping of mouse cells onto human clusters was performed using Seurat multimodal reference mapping. To run, the mouse data was prepared by extracting the counts matrix from the mouse sNuc object and mapping the mouse gene names to their human orthologs. The mouse object was then split by sample and mapped onto the human object using the RNA assay and PCA reduction.

Gene Pathway Analysis
Analysis of enriched pathways in adipocyte markers was performed using clusterProfiler (version 3.16.1). Adipocyte cluster markers were filtered to an adjusted p-value of less than .05, then evaluated for enrichment in GO biological pathways or KEGG pathways containing under 300 genes.

Identification and analysis of EBF2 SNP association with visceral adiposity
VAT, ASAT, and GFAT volumes in 40,032 individuals from the UK Biobank who underwent MRI imaging were quantified as described elsewhere. Variant rs4872393 was identified as a lead SNP associated with VATadj and waist-to-hip ratio from summary statistics of two prior studies. Among the cohort who underwent MRI imaging, all variants at this locus (± 250 kb around rs4872393) with MAF >= 0.005 and imputation quality (INFO) score >= 0.3 were analyzed. For all 554 nominally significant ($P < 0.05$) variants associated with VATadjBMI in this region, a secondary conditional analysis testing for association with VATadj was performed controlling for rs4872393 carrier status ($P < 0.05/554 = 9 \times 10\text{-}5$). Participants were excluded from analysis if they met any of the following criteria: (1) mismatch between self-reported sex and sex chromosome count, (2) sex chromosome aneuploidy, (3) genotyping call rate < 0.95, or (4) were outliers for heterozygosity. Up to 37,641 participants were available for analysis. Fat depot volumes adjusted for BMI and height ("adj" traits) were calculated by taking the residuals of the fat depot in sex-specific linear regressions against age at the time of MRI, age squared, BMI, and height. Each trait was scaled to mean 0 and variance 1 in sex-specific groups before being combined for analysis. Linear regressions between a given trait-variant pair were adjusted for age at the time of imaging, age squared, sex, the first 10 principal components of genetic ancestry, genotyping array, and MRI imaging center. Analyses were performed using R 3.6.0 (R Project for Statistical Computing). EBF2 regional visualization plot was made with the LocusZoom online tool.

Calculation of pseudobulk datasets to estimate adipose innervation
Approximate bulk RNA-seq datasets (pseudobulk) were obtained for visceral sNuc-seq samples by summing the total expression per-gene across all droplets containing a valid 10X cell barcode. This includes all cells that would normally have been removed in the single-nuclei studies by any of the filtering criteria (above): doublet score, splicing content, droplets with fewer than 400 UMIs, etc, in order to preserve the ambient RNA present in otherwise empty droplets. Repeated UMIs were still collapsed into single counts (per-droplet) before summing. Levels of pan-neuronal markers were calculated using this pesudobulk dataset and plotted against the proportion of visceral populations hAd2 and hAd6 relative to total adipocytes in each sample.

Prediction of cell-cell interactions
Analysis of cell-cell interactions was performed using CellphoneDB (version 2.0.0). For human data, sNuc-seq counts data was split into files containing cells from subcutaneous and visceral fat from individuals with BMI lower or higher than 30. CellphoneDB with statistical analysis was run on each file separately to evaluate interactions in each condition. For mouse data, counts data was split into files containing cells from the inguinal and epididymal fat of chow and high fat diet fed mice. Mouse gene names were converted to human gene names, as above, before running CellphoneDB with statistical analysis on each file.

Identification of candidate etiologic cell types using CELLEX and CELLECT
CELLECT (https://github.com/perslab/CELLECT) and CELLEX (https://github.com/perslab/CELLEX) were used to identify candidate etiological cell types for traits with available GWAS studies. The input data for CELLECT is GWAS summary statistics for a given trait and cell type expression specificity (ES) estimates derived from single-cell RNA-seq data. The output is a list of prioritized candidate etiologic cell types for a given trait. ES estimates were calculated using CELLEX (version 1.1), which computes robust estimates of ES by relying on multiple expression

specificity measures (for further details see Timshel et. al.). CELLEX was run separately on the raw mouse and human (sNuc) gene expression matricies to compute gene expression specificities for each cluster based on the clustering assignment reported above. The resulting cell type specificity matrix was used along with multiple GWAS studies41, (Extended Data Table 3) as input for CELLECT (version 1.1), which was run with default parameters. Significant cell types were identified using a by-trait and by-species Bonferroni p-value threshold of p<0.05.

SNP analysis for bulk mRNA-seq cohort
The raw GTC SNP expression data from Infinium OmniExpress-24 Kit was converted to VCF format using Picard version 2.21.6. The pre-processing of the SNP data before phasing and imputation was performed using plink2 (https://www.cog-genomics.org/plink/2.0/). The SNP genotype was then phased and imputed using the Eagle v2.3.5 (http://eagle.r-forge.r-project.org/index.html) and Minimac370 packages, respectively. SNPs were mapped to the NCBI database using the rsnps package (https://CRAN.R-project.org/package=rsnps) and filtered to keep only SNPs that had a minor allele frequency > 0.05. For plotting gene expression against genotype, bulk RNA sequencing data was TMM normalized using edgeR. Statistical validation for significance was done using the Wilcoxon rank-sum Test which is a non-parametric test assuming independent samples.

Statistics
p-values for scatterplots were calculated using GraphPad Prism version 8.0 and represent the results of an extra sum-of-squares F-test with the null hypothesis that the slope equals zero. All error bars on bar graphs represent standard error. Statistics on proportional composition graphs were calculated using scCODA83 (version 0.1.2) using the Hamiltonian Monte Carlo sampling method. The model formula used was "Depot + BMI" (human) or "Depot + Diet) (mouse) for all objects in for which both of these covariates were present, or the individual covariate when only a single condition was present.

For manuscripts utilizing custom algorithms or software that are central to the research but not yet described in published literature, software must be made available to editors and reviewers. We strongly encourage code deposition in a community repository (e.g. GitHub). See the Nature Research guidelines for submitting code & software for further information.

Data

Policy information about availability of data

All manuscripts must include a data availability statement. This statement should provide the following information, where applicable:

- Accession codes, unique identifiers, or web links for publicly available datasets
- A list of figures that have associated raw data
- A description of any restrictions on data availability

Single cell RNA expression and count data is deposited in the Single Cell Portal (Study #SCP1376). Processed count data for bulk RNA-seq and dge matrices for single cell and single nucleus RNA-seq have been deposited in GEO (Bulk-seq Accession #GSE174475, sc-RNA-seq Accession # GSE176067, sNuc-sec Acession #GSE176171), raw sequencing reads for mouse data are available in SRA, study #SRP322736. FASTQ and SNP array files for human samples are deposited in dbGaP, Accession #phs002766.v1.p1. Publicaly available datasets and databases used were the following: METSIM RNA-seq data from Raulerson et. al.13 (GSE135134); single cell ASPC data from Burl et. al.4 (SRP145475), Hepler et. al.6 (GSE111588), Merrick et. al.5 (GSE128889), Sárvári et. al.9 (GSE160729), and Schwalie et. al.3 (E-MTAB-6677); human assembly GRCh38 and GENCODE annotation 27 (https://www.gencodegenes.org/human/release_27.html); mouse assembly GRCm38 and GENCODE annotation M16 (https://www.gencodegenes.org/mouse/release_M16.html).

Field-specific reporting

Please select the one below that is the best fit for your research. If you are not sure, read the appropriate sections before making your selection.

☒ Life sciences ☐ Behavioural & social sciences ☐ Ecological, evolutionary & environmental sciences

For a reference copy of the document with all sections, see nature.com/documents/nr-reporting-summary-flat.pdf

Life sciences study design

All studies must disclose on these points even when the disclosure is negative.

Sample size	For human studies, no sample size calculations were performed, sample size was determined by the availability of patient samples and by the cost involved in single cell sequencing. For mouse studies, no sample size calculations were performed, sample size was determined by the cost involved in single cell sequencing, and the acquisition of a target number of cells (approximately 100k cells per depot)
Data exclusions	Some samples were excluded from the final analysis due to poor quality control metrics (ie too few reads in cells). Of samples that passed the QC metrics, one mouse inguinal sample was removed due to a the presence of a large proportion of T/NK cells, believed to be from the lymph node present in the inguinal adipose tissue. Within samples, cells were removed if they did not pass QC metrics: >400 UMIs, less than 10% mitochondrial read percent, not predicted to be a doublet, (for human sNuc only) spliced/unspliced read percent less than 75%. Of cells that initially passed QC metrics, some were later removed because they were contained in clusters that appeared to be doublets or that appeared to be driven by high levels of ambient RNA.
Replication	For humans, individuals are considered replicates- we had an n of 9 scRNA-seq and 13 sNuc-seq individuals. Mice were also treated as individuals, we have an n of 7 chow and 7 HFD mice in this dataset. Notably, all clusters and subclusters presented here were comprised of cells from more than one individual. All clusters and subclusters identified in this paper were found in all biological replicates- ie a cluster enriched in human visceral high BMI samples was found in all such samples, thus we consider all attempts at replication to be successful.
Randomization	Male mice were purchased from Jackson Labs after being fed chow or HFD for 16 weeks, thus the decision to feed chow or HFD was not made by the researchers. Female mice were purchased at 6 weeks old and weighed only after assignment to chow or HFD groups to ensure random

assignment. All other studies contained no randomization. Because this was not an interventional study but rather a description of the cell types found across individuals, randomization was not relevant to our experiments.

Blinding

The investigators were not blinded to subject metadata in the human or mouse experiments. Because this was not an interventional study but rather a description of cell types found in the adipose tissue and how those cell types change across depot and diet/BMI, it was not possible to perform this analyses while blinded and blinding was not relevant for this study.

Reporting for specific materials, systems and methods

We require information from authors about some types of materials, experimental systems and methods used in many studies. Here, indicate whether each material, system or method listed is relevant to your study. If you are not sure if a list item applies to your research, read the appropriate section before selecting a response.

Materials & experimental systems

n/a	Involved in the study
☐	☒ Antibodies
☒	☐ Eukaryotic cell lines
☒	☐ Palaeontology and archaeology
☐	☒ Animals and other organisms
☐	☒ Human research participants
☒	☐ Clinical data
☒	☐ Dual use research of concern

Methods

n/a	Involved in the study
☒	☐ ChIP-seq
☒	☐ Flow cytometry
☒	☐ MRI-based neuroimaging

Antibodies

Antibodies used

GRIA4, 1:200, Cat #23350-1-AP, Proteintech
PGAP1, 1:400, Cat. #55392-1-AP, Proteintech
EBF2, 1:1000, Cat. #AF7006, R&D systems
AGMO (TMEM195) 1:100, Cat #orb395684, Biorbyt
Alexa Fluor 546, 1:500, Cat. #A-11035, ThermoFisher

Validation

GRIA4: the manufacturers have shown validation of the antibody by using it to perform western blotting and IHC in rat and mouse brain. The antibody was further validated by the researchers by staining in mouse brain as a positive control, positivity was found in some cerebral cortex pyramidal neurons
PGAP1: the manufacturers have shown validation of the antibody by using it to perform western blotting and IHC in human testis. The antibody was further validated by the researchers by staining in human testicle as a positive control, staining was found mainly in germinal stem cells
EBF2: the manufacturers have shown validation of the antibody by using it perform western blotting in 3t3-L1 cells and IHC in mouse embryo. The antibody was further validated by the researchers by staining in mouse embryo as a positive control, staining was found in the nuclei of multiple cell types.
AGMO: the manufacturers have shown validation of the antibody by using to perform western blotting in MCF-7 cells and IHC in human liver tissue. The antibody was further validated by the researchers by staining in human liver as a positive control, staining was found primarily in hepatocytes.
Alexa Fluor 546: the manufacturers have shown validation of the antibody by using it to perform imunofluorescence analysis on HeLa cells stained with a rabbit alpha Tubulin antibody.

Animals and other organisms

Policy information about studies involving animals; ARRIVE guidelines recommended for reporting animal research

Laboratory animals

The study used 19 week old C57BL/6 male and female mice that had been maintained on chow diet or high fat diet, starting at 6 weeks of age.

Wild animals

The study did not involve wild animals.

Field-collected samples

The study did not involve samples collected from the field.

Ethics oversight

All animal studies were approved by the Beth Israel Deaconess Medical Center Institutional Animal Care and Use Committee.

Note that full information on the approval of the study protocol must also be provided in the manuscript.

Human research participants

Policy information about studies involving human research participants

Population characteristics

Participants were female and male subjects undergoing abdominal surgery. The broad classes or surgeries included in this study are plastic surgery, gynecological surgery, GI-related surgery, and bariatric surgery. As such, many participants had medical conditions related to those surgeries. The participants ranged in age from 24-73 years old.

Recruitment	Participants were recruited from surgery rosters of surgeons performing (abdominal) plastic, bariatric, GI, and gynecological surgeries. Participants were approached in the preoperative room, asked if they were willing to participate in the study, and if so, provided further information about the study and informed consent. Patients who could not communicate well in English were not included in this study as the resources were not available to give informed consent in other languages, thus the patient population was biased towards English speakers which may have influenced the races and ethnicities included in this study. We do not expect this to greatly impact the results of this study.
Ethics oversight	Human studies were approved by the Institutional Review Boards at Beth Israel Deaconess Medical Center, the University of Pittsburgh Medical Center, or the Technical University of Munich.

Note that full information on the approval of the study protocol must also be provided in the manuscript.